


The Respective Roles of Ocean Heat Transport and Surface Heat Fluxes in Driving Arctic Ocean Warming and Sea Ice Decline

DYLAN OLDENBURG^{},^a YOUNG-OH KWON,^a CLAUDE FRANKIGNOUL,^{b,a} GOKHAN DANABASOGLU,^c STEPHEN YEAGER,^c AND WHO M. KIM^c

^a Woods Hole Oceanographic Institution, Falmouth, Massachusetts

^b Sorbonne University, LOCEAN/IPSL, Paris, France

^c National Science Foundation National Center for Atmospheric Research, Boulder, Colorado

(Manuscript received 3 July 2023, in final form 3 November 2023, accepted 12 December 2023)

ABSTRACT: Arctic Ocean warming and sea ice loss are closely linked to increased ocean heat transport (OHT) into the Arctic and changes in surface heat fluxes. To quantitatively assess their respective roles, we use the 100-member Community Earth System Model, version 2 (CESM2), Large Ensemble over the 1920–2100 period. We first examine the Arctic Ocean warming in a heat budget framework by calculating the contributions from heat exchanges with atmosphere and sea ice and OHT across the Arctic Ocean gateways. Then we quantify how much anomalous heat from the ocean directly translates to sea ice loss and how much is lost to the atmosphere. We find that Arctic Ocean warming is driven primarily by increased OHT through the Barents Sea Opening, with additional contributions from the Fram Strait and Bering Strait OHTs. These OHT changes are driven mainly by warmer inflowing water rather than changes in volume transports across the gateways. The Arctic Ocean warming driven by OHT is partially damped by increased heat loss through the sea surface. Although absorbed shortwave radiation increases due to reduced surface albedo, this increase is compensated by increasing upwelling longwave radiation and latent heat loss. We also explicitly calculate the contributions of ocean–ice and atmosphere–ice heat fluxes to sea ice heat budget changes. Throughout the entire twentieth century as well as the early twenty-first century, the atmosphere is the main contributor to ice heat gain in summer, though the ocean's role is not negligible. Over time, the ocean progressively becomes the main heat source for the ice as the ocean warms.

SIGNIFICANCE STATEMENT: Arctic Ocean warming and sea ice loss are closely linked to increased ocean heat transport (OHT) into the Arctic and changes in surface heat fluxes. Here we use 100 simulations from the same climate model to analyze future warming and sea ice loss. We find that Arctic Ocean warming is primarily driven by increased OHT through the Barents Sea Opening, though the Fram and Bering Straits are also important. This increased OHT is primarily due to warmer inflowing water rather than changing ocean currents. This ocean heat gain is partially compensated by heat loss through the sea surface. During the twentieth century and early twenty-first century, sea ice loss is mainly linked to heat transferred from the atmosphere; however, over time, the ocean progressively becomes the most important contributor.


KEYWORDS: Arctic; Sea ice; Climate; Climate change; Climate models; Oceanic variability

1. Introduction

The Arctic has been warming much more rapidly than the global average over the past few decades (e.g., Serreze et al. 2009; Marshall et al. 2014; Pithan and Mauritsen 2014; Huang et al. 2017; Chylek et al. 2022; Rantanen et al. 2022), a phenomenon known as Arctic Amplification. As a result, sea ice extent and thickness have decreased dramatically in recent decades (Onarheim et al. 2018; Stroeve and Notz 2018; Previdi et al. 2021). This warming and associated sea ice loss have had severe impacts on Arctic ecosystems. These impacts are widely expected to intensify in the near future (e.g., Johannessen and Miles 2011; Vincent et al. 2011; Fu et al.

2020; Grémillet and Descamps 2023). Arctic warming and sea ice decline may also be impacting Eurasian and North American midlatitude weather patterns (Honda et al. 2009; Kim et al. 2014; Francis et al. 2017), though this is still heavily debated (e.g., Overland et al. 2016; Blackport et al. 2019; Screen and Blackport 2019).

It has become increasingly clear that Arctic Ocean warming and associated sea ice loss are closely linked to increased ocean heat transport (OHT) through the Fram Strait and Barents Sea Opening (BSO) (Onarheim et al. 2015; Polyakov et al. 2017; Auclair and Tremblay 2018; Stroeve and Notz 2018; Wang et al. 2020; Chemke et al. 2021; Shu et al. 2022). This process, known as Atlantification, is robust across recent observations and global climate model simulations (Stroeve and Notz 2018; van der Linden et al. 2019; Asbjørnsen et al. 2020; Timmermans and Marshall 2020; Shu et al. 2022). Between 1980 and 2012, Atlantic Water temperatures at Fram Strait and the BSO have warmed by approximately 1°–1.5°C (Muilwijk et al. 2018). Meanwhile, in the Eurasian basin, estimated vertical heat fluxes from the Atlantic Water layer were

 Denotes content that is immediately available upon publication as open access.

Corresponding author: Dylan Oldenburg, dylan.oldenburg@who.edu

DOI: 10.1175/JCLI-D-23-0399.1

© 2024 American Meteorological Society. This published article is licensed under the terms of the default AMS reuse license. For information regarding reuse of this content and general copyright information, consult the AMS Copyright Policy (www.ametsoc.org/PUBSReuseLicenses).

Brought to you by MBL/WHOI Library | Unauthenticated | Downloaded 01/26/24 08:57 PM UTC

approximately 2–4 times greater in 2014/15 than in 2007/08 (Polyakov et al. 2017). Enhanced heat transport through the BSO has been found to explain most of the recent observed Barents Sea warming and sea ice changes (Årthun et al. 2012; Smedsrud et al. 2013). This warming and sea ice loss are expected to intensify based on model predictions (e.g., Onarheim and Årthun 2017; Årthun et al. 2019; Polyakov et al. 2020; Shu et al. 2021, 2022). This OHT is also expected to strengthen over time due to local circulation changes and warmer inflowing water (e.g., Oldenburg et al. 2018; van der Linden et al. 2019).

Similarly, on the Pacific side of the Arctic, OHT through the Bering Strait has increased from 10 to 16 TW between 2001 and 2014 due to enhanced volume transport and warmer inflowing water, a process known as Pacification (Woodgate et al. 2015; Woodgate 2018; Polyakov et al. 2020; Timmermans and Marshall 2020). This stronger OHT contributes to the rapid warming and sea ice decline in the Chukchi Sea (Woodgate et al. 2010), as well as the warming of the upper ocean in the Canada basin (Woodgate 2018; Polyakov et al. 2020). Some of this extra heat in the Chukchi Sea is stored in the Beaufort Gyre halocline, and could melt nearly 1 m of sea ice if released to the surface (Timmermans and Marshall 2020).

While Arctic sea ice evolution is influenced by changes in OHT from the Atlantic and Pacific, it is not yet clear how much of the heat accumulated due to OHT is used to melt the sea ice and how much is released to the atmosphere. Furthermore, surface heat fluxes from the atmosphere also contribute to sea ice changes. In particular, enhanced absorbed shortwave radiation as a result of reduced surface albedo further accelerates sea ice decline via the ice-albedo feedback (e.g., Manabe and Stouffer 1980; Holland and Bitz 2003; Winton 2006; Pithan and Mauritsen 2014; Hu et al. 2017; Hwang et al. 2018). Because this additional radiative flux occurs in summer, it can also delay the onset of ice growth in autumn, while the heat gained by the ocean is released to the atmosphere as longwave radiation as well as sensible and latent heat (Screen and Simmonds 2010; Previdi et al. 2021). This process can also lead to further melting of sea ice by warming the atmosphere and increasing cloud cover, and enhancing downwelling longwave radiation as a result (Previdi et al. 2021).

In this paper, we first seek to understand how the heat budget of the Arctic Ocean will change in the future as well as how it has changed over the historical period due to the external forcing using a large ensemble of simulations of a state-of-the-art fully coupled Earth system model. To do this, we quantify the heat inputs and outputs into and out of the Arctic Ocean basin, i.e., the lateral OHT and sea surface heat fluxes. Then we determine how much each Arctic gateway contributes to the total OHT into the Arctic, and decompose the sea surface heat flux into its components. We next ascertain how much volume transport and temperature changes contribute to OHT changes across the Arctic gateways. We also determine how much heat from the ocean contributes to sea ice melt and how much is released to the atmosphere.

Second, we focus on the heat budget from the sea ice perspective. The goal here is to understand whether the atmosphere–ice

or the ocean–ice fluxes are more important in driving Arctic sea ice decline.

2. Community Earth System Model, version 2

a. Model description

In our analyses, we use the 100-member ensemble of historical and future simulations of the standard resolution Community Earth System Model, version 2 (CESM2; Danabasoglu et al. 2020), known as the CESM2 Large Ensemble (CESM2-LENS; Rodgers et al. 2021). All CESM2 components have a nominal spatial resolution of 1°. Each ensemble member was run with historical forcing for 1850–2014, then subsequently driven by SSP3-7.0 forcing over years 2015–2100 as defined for CMIP6 (Eyring et al. 2016). Ensemble spread was achieved by a combination of micro- and macro-initialization approaches using initial conditions between years 1001 and 1301 of the CESM2 preindustrial control simulation, during which the top of atmosphere global energy imbalance and model drift were both small (Danabasoglu et al. 2020). Specifically, states for years 1231, 1251, 1281, and 1301 were used as initial conditions for four sets of 20-member ensembles where round-off level perturbations were used in the initial atmospheric potential temperature field to generate spread. The remaining 20 members were initialized using states that are 10 years apart during years 1001–1191 of the preindustrial control simulation. No other perturbations were used for these members. Two different biomass burning forcing fields were applied, each to half of the simulations. For the first 50 members, biomass burning is represented as given in the CMIP6 protocols. For the remaining 50 members, biomass burning emissions were smoothed with an 11-yr moving average filter, substantially reducing variability in aerosol fluxes between 1990 and 2020 without changing the time mean (Rodgers et al. 2021) and significantly impacting the simulation of Northern Hemisphere extratropical climate in the early twenty-first century (Fasullo et al. 2022).

A major benefit of using such a large number of ensemble members is that it allows us to more robustly separate externally forced variability from internal variability in the model (Deser et al. 2012; Årthun et al. 2019; Deser et al. 2020). In such large ensembles, the forced response of a variable can be approximated by averaging its evolution across various ensemble members, while the ensemble spread gives information on the internal variability intrinsic to the model (e.g., Deser et al. 2012, 2020). Given that there are minimal changes in the ocean and sea ice heat budgets up until the mid-twentieth century (Figs. 1c,d), in this analysis we focus on the period between 1920 and 2100.

b. Variables used

For this paper, we exclusively use monthly mean model output from the ocean, atmospheric and sea ice components. For the ocean heat budget, we use velocity and potential temperature to calculate the heat transports and ocean heat content. For the sea surface heat fluxes, we use net shortwave radiation fluxes, downwelling and upwelling longwave radiation fluxes, sensible and latent heat fluxes, heat fluxes from

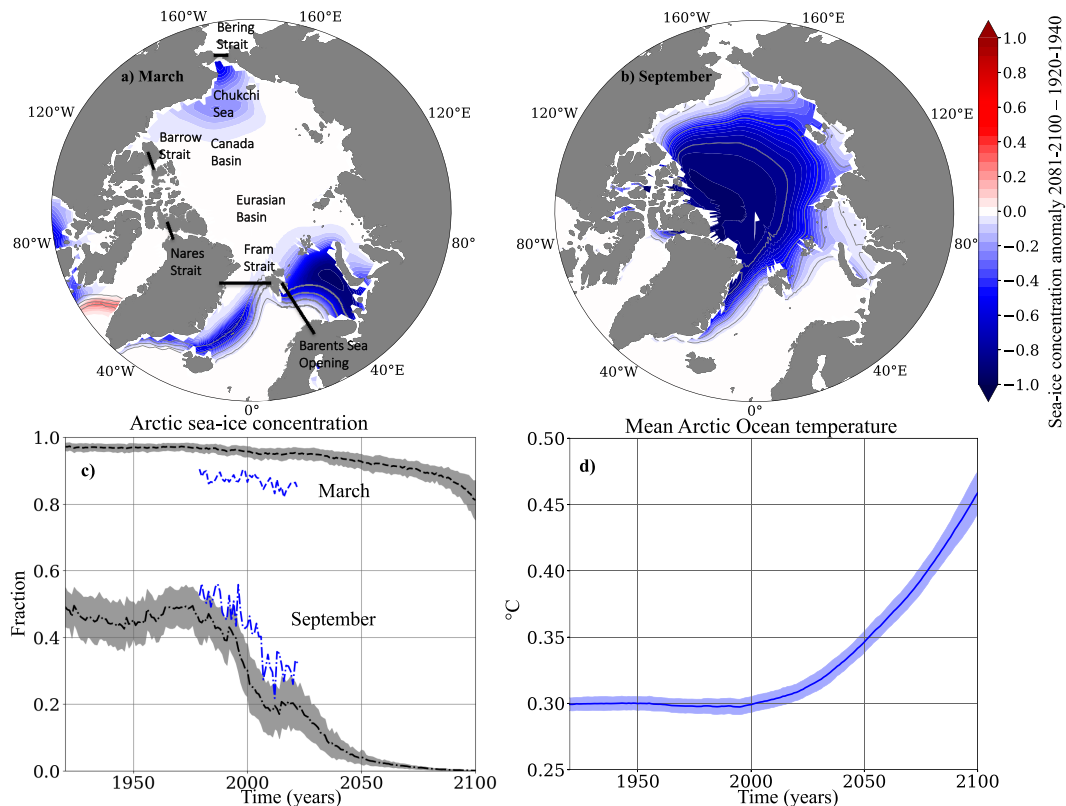


FIG. 1. (top) Ensemble mean Arctic sea ice concentration anomalies for 2081–2100 relative to 1920–40 (colors) and mean Arctic sea ice concentration for 1920–40 (contours) from CESM2-LENS for (a) March and (b) September. The thick contours are for 5%, 20%, 50%, and 80%. (c) Ensemble mean (black) and observational (blue) Arctic sea ice concentration time series for March (dashed line) and September (dot-dash line). Shading represents one standard deviation across ensemble members. The observational sea ice concentration is derived from the NOAA/NSIDC Climate Data Record of Passive Microwave Sea Ice Concentration, version 4 (Meier et al. 2021). (d) Annual-mean volume-mean Arctic Ocean temperature time series.

snow and frozen runoff and heat fluxes associated with formation and melting of sea ice, including frazil ice formation in the ocean model when the surface temperatures dip below the salinity-dependent freezing point. Because these sea surface heat fluxes are all taken from the ocean model output, they include interactions between the ocean and both the atmosphere and ice.

For the Arctic sea ice heat budget, we use monthly mean output from the sea ice model. The model provides the net ocean–ice heat flux, the net shortwave radiation and that transmitted to the ocean, the downwelling and upwelling longwave radiation fluxes, and the atmosphere–ice latent and sensible heat fluxes.

For our analysis of longwave radiation fluxes, we use atmospheric monthly mean output of cloud fraction and specific humidity taken at 920 hPa alongside sea ice output of surface snow/ice temperature. We choose 920 hPa when analyzing humidity because we are interested in the humidity in the lower atmosphere. Choosing a higher or lower pressure does not significantly affect the result.

It is standard practice to remove preindustrial control simulations trends from all variables prior to analysis (Gupta et al. 2012).

These trends can be determined from the preindustrial control simulations from which the CESM2-LENS runs are branched. The associated trends in the variables used here are assumed to be very small and are hence neglected in this analysis.

c. Model evaluation

First, we discuss the general performance of the CESM2 model, then we analyze biases in the CESM2-LENS simulations. The stratification in the Arctic Ocean is poorly represented in CESM2, though it does not perform particularly poorly compared to other low-resolution CMIP6 models (Heuzé et al. 2023). It also exhibits large temperature biases in the Fram Strait, with a cold bias in the upper layer and a warm bias in the deeper layers (Heuzé et al. 2023).

In CESM2-LENS, the Arctic sea ice extent is underestimated in September, and overestimated in March compared to observational estimates (Fig. 1c). The net volume transports through the three Arctic gateways are well-represented relative to observations (Table 1). The mean strength of the net flow through the Fram Strait over years 1997–2006 is equal to -1.6 ± 0.8 Sv ($1 \text{ Sv} \equiv 10^6 \text{ m}^3 \text{ s}^{-1}$), which is in line with observations over that period (-2.0 ± 2.7 Sv,

TABLE 1. Net ocean volume transports and their standard deviations (Sv) across three Arctic gateways from CESM2-LENS and observations. Transports for the Fram Strait and BSO are calculated over years 1997–2007 while transports for the Bering Strait are calculated over years 1990–95 in order to allow for proper comparison to observations. Observation values for Fram Strait transports are taken from Schauer et al. (2008) and Timmermans and Marshall (2020). Values for the Barents Sea Opening and Bering Strait are from Roach et al. (1995), Woodgate and Aagaard (2005), Skagseth et al. (2008), Smedsrud et al. (2010), Beszczynska-Möller et al. (2011), Mauritzen et al. (2011), and Smedsrud et al. (2013). Values for the Barrow Strait are from Schauer et al. (2008) and are calculated from 1998 to 2004. Positive and negative values indicate northward and southward transports, respectively.

Name	CESM2-LENS	Observations
Fram Strait	-1.6 ± 0.8	-2.0 ± 2.7
Barents Sea Opening	2.1 ± 0.9	~ 2.3
Bering Strait	1.1 ± 0.2	0.8 ± 0.2
Barrow Strait	-0.2 ± 0.03	-1

Schauer et al. 2008; Timmermans and Marshall 2020). The mean volume transports through the Bering Strait (1.1 ± 0.2 Sv) and BSO (2.1 ± 0.9 Sv) also align well with observations (0.8 ± 0.2 Sv and ~ 2.3 Sv, respectively; Roach et al. 1995; Woodgate and Aagaard 2005; Skagseth et al. 2008; Smedsrud et al. 2010; Beszczynska-Möller et al. 2011; Mauritzen et al. 2011; Smedsrud et al. 2013). These values can also be compared to multimodel mean volume transports from ocean–sea ice models forced by the interannually varying atmospheric datasets as part of the Coordinated Ocean-ice Reference Experiments, phase II (CORE-II; Wang et al. 2016). These values align well with those from CESM2-LENS. This comparison can be seen in Table 2.

The heat transports across the BSO and the Bering Strait also align well with observations, but the Fram Strait OHT is underestimated (Tables 3 and 4). Specifically, the CESM2-LENS BSO OHT value is equal to 0.04 ± 0.02 PW, while the corresponding observational estimate over the same period is equal to ~ 0.05 PW (Schauer et al. 2008). For the Bering Strait, the observational estimates from Woodgate et al. (2015) and Woodgate (2018) are calculated with a reference temperature of -1.9°C . Using this reference temperature in our Bering Strait OHT calculation yields a somewhat higher heat transport, i.e., 0.013 ± 0.002 PW, which is in line with the observational values (Woodgate et al. 2015; Woodgate 2018). The heat transport across the Fram Strait in CESM2-LENS over years 1997–2008 is equal to 0.01 ± 0.01 PW, much lower than what is found in observations (0.04 ± 0.01 PW; Schauer et al. 2008; Rudels et al. 2015; Timmermans and Marshall 2020). These heat transports can also be compared with CMIP6 multimodel mean values from Shu et al. (2022). The multimodel mean Fram Strait OHT is closer to observations than CESM2-LENS, while the BSO OHT in CESM2-LENS is more in line with observations than the CMIP6 multimodel mean values. The Bering Strait OHT in CESM2-LENS is the same as the multimodel mean (Table 3).

TABLE 2. Net ocean volume transports and their standard deviations (Sv) across three Arctic gateways from CESM2-LENS and CORE-II over 1978–2007. CORE-II values are from Wang et al. (2016).

Name	CESM2-LENS	CORE-II
Fram Strait	-1.5 ± 0.8	-2.2
Barents Sea Opening	2.0 ± 0.9	2.7
Bering Strait	1.1 ± 0.2	1.0

3. Arctic Ocean heat budget

For our heat budget analysis, we define the Arctic Ocean as the region bounded by the Arctic gateways, which include the Nares Strait, Fram Strait, BSO, Bering Strait, and Barrow Strait (Fig. 1a).

The Arctic Ocean heat budget is defined as

$$\frac{d}{dt} \text{OHC} = \rho c_p \frac{dT}{dt} = \text{OHT}_{\text{tot}} + \text{SHF} + \text{QFLUX} + F_{\text{residual}}, \quad (1)$$

where $\rho = 1027.5 \text{ kg m}^{-3}$ represents the seawater density, $c_p = 4186 \text{ J kg}^{-1} \text{ K}^{-1}$ refers to the heat capacity of seawater, OHC is the ocean heat content, OHT_{tot} is the total OHT into the Arctic, SHF is the sea surface heat flux including heat exchanges with both the atmosphere and sea ice, and QFLUX is the heat flux due to frazil ice formation.

The total OHT (OHT_{tot}) is the sum of the Eulerian-mean OHT (OHT_{Eul}) and submonthly transient OHT (OHT_{subm}), which are defined as follows:

$$\text{OHT}_{\text{tot}}(t) = \rho c_p \int_{x_1}^{x_2} \int_{z_{\text{bot}}}^0 \bar{v} \bar{\theta} dz dx, \quad (2)$$

$$\text{OHT}_{\text{Eul}}(t) = \rho c_p \int_{x_1}^{x_2} \int_{z_{\text{bot}}}^0 \bar{v} \bar{\theta} dz dx, \quad (3)$$

$$\text{OHT}_{\text{subm}}(t) = \rho c_p \int_{x_1}^{x_2} \int_{z_{\text{bot}}}^0 \bar{v} \bar{\theta} dz dx - \rho c_p \int_{x_1}^{x_2} \int_{z_{\text{bot}}}^0 \bar{v} \bar{\theta} dz dx, \quad (4)$$

where v represents the velocity; θ represents the potential temperature, x , z , and t represent the horizontal spatial coordinate, depth, and time, respectively; x_1 and x_2 represent the spatial boundaries of the sections; ρ represents the seawater density; c_p refers to the heat capacity of seawater; and z_{bot} represents the bottom depth.

There is also a residual term between the OHC change and the other terms, which represents the parameterized bolus eddy and diffusion ocean heat transport as well as any error due to our usage of monthly mean data. This is defined as follows:

$$F_{\text{residual}} = \frac{d}{dt} \text{OHC} - \text{OHT}_{\text{tot}} - \text{QFLUX} - \text{SHF}. \quad (5)$$

a. Ocean heat and volume transports across Arctic gateways

When calculating the OHT into the Arctic, previous studies have typically used zonally integrated OHT across a particular

TABLE 3. Net model resolved ocean heat transports and their standard deviations (PW) across three Arctic gateways from CESM2-LENS, CMIP6, and observations. Fram Strait OHT is calculated over years 1997–2008, BSO OHT is calculated over 1997–2007, and Bering Strait OHT is calculated for 1998–2014. The CESM2-LENS values are referenced to 0°C. CMIP6 multimodel mean values are taken from Fig. 4 in Shu et al. (2022), which are referenced to 0°C. Observational values are from Schauer et al. (2008), Rudels et al. (2015), Woodgate et al. (2015), Woodgate (2018), and Timmermans and Marshall (2020).

Name	CESM2-LENS	CMIP6 multimodel mean	Observations
Fram Strait	0.01 ± 0.01	0.02	0.04 ± 0.01
Barents Sea Opening	0.04 ± 0.02	0.07	~0.05
Bering Strait	0.01 ± 0.01	0.01	0.01–0.02
Barrow Strait	0.001 ± 0.0002	–	0.003

latitude, e.g., 65°N or 70°N (Mahlstein and Knutti 2011; Screen et al. 2012; Koenigk and Brodeau 2014; Sun et al. 2015). However, the choice of a latitude is somewhat arbitrary because the selection is not based on physical pathways into the Arctic, and OHT varies substantially depending on which latitude is chosen. Here we instead explicitly calculate the OHT across each Arctic gateway (Fig. 1a). Because these sections define a closed Arctic domain, they allow us to do heat budget calculations. Obtaining these OHTs separately also means that we can determine their relative importance across individual Arctic gateways.

To calculate the Eulerian-mean OHT $[\overline{v\theta}]$, where the overbar denotes the monthly mean; Eq. (1)] across these sections, we use the Physical Analysis of the Gridded Ocean (PAGO) code from Deshayes et al. (2014). PAGO uses monthly mean velocity and temperature to calculate heat and volume transports across defined sections. The OHT and volume transports are then annually averaged. While the volume transports are not strictly necessary to calculate the heat budget, they aid in understanding what drives the OHT variability. Note that the OHT calculated by PAGO does not include the submonthly transient OHT by the explicitly resolved flows or the OHT by parameterized eddy contributions, because we only use monthly mean velocity and potential temperature.

We then separately calculate the submonthly transient covariance term of OHT $[v'\theta']$; Eq. (2), where the prime denotes the submonthly anomalies defined as the deviation from the monthly mean] as a residual from the model output total ocean heat flux $[\overline{v\theta}]$; Eq. (3)] by the resolved flow, which is calculated during model integration at each model time step, and the Eulerian-mean OHT $(\overline{v\theta})$. Note that this does not include OHT due to any parameterized flows, i.e., the bolus and diffusive OHT, which can be approximated as the residual between the Arctic ocean heat content (OHC) change and the sum of the Eulerian-mean and submonthly transient components and all the surface fluxes [Eq. (4)].

TABLE 4. Model resolved inflow and outflow ocean heat transports and their standard deviations (PW) across Fram Strait from CESM2-LENS and observations calculated over years 1997–2008. The CESM2-LENS values are referenced to 0°C. Observational values are from Fahrback (2006).

Name	CESM2-LENS	Observations
Inflow	0.02 ± 0.002	0.06 ± 0.02
Outflow	-0.01 ± 0.002	-0.02 ± 0.01

When calculating OHT across segments with a nonzero mass flux, it is typically best practice to use the mean temperature of the domain as a reference rather than 0°C (Lee et al. 2004). However, because our calculation of the submonthly transient OHT relies on model output ocean heat flux $(\overline{v\theta})$, which is effectively referenced to 0°C, we must also use 0°C here for consistency.

All of the heat flux components remain approximately constant in the ensemble mean until around 1980 (Fig. 2a). The ensemble mean total OHT into the Arctic then starts to increase, strengthening from 0.06 PW averaged over years 1961–80 to 0.10 PW for 2081–2100. This more than overwhelms the increase in surface heat loss, which changes from –0.06 to –0.08 PW (Fig. 2a). As a result, the Arctic OHC increases monotonically from 1995 onward. By 2081–2100, the OHC tendency reaches 0.02 PW. The total OHC change over the course of the simulations increases the mean Arctic Ocean temperature from 0.30° to 0.46°C (Fig. 1d). In summary, the increase in the OHT into the Arctic in response to the external forcing results in an Arctic temperature increase which is partly damped by the enhanced heat loss through the sea surface, as found in other climate models (Shu et al. 2022).

Interestingly, the standard deviations in OHC tendency, OHT and surface heat flux across ensemble members also increase over time. The OHC tendency standard deviation changes from 0.007 PW in 1961–80 to 0.017 PW in 2081–2100, while the total OHT and surface heat flux standard deviations increase from 0.008 to 0.015 PW and 0.008 to 0.016 PW over the same period, respectively. Also, when the changes in the standard deviations are normalized by the changes in their respective ensemble mean values, the standard deviation of OHT changes very little over time. This indicates that the standard deviation and mean values vary together. However, for the SHF, the standard deviation continues to increase despite the ensemble mean value remaining essentially constant after 2060.

When the subcomponents of OHT are considered, the ensemble mean total OHT change is dominated by the changes in the Eulerian-mean OHT, which increases from 0.05 PW in 1961–80 to 0.08 PW over 2081–2100 (Fig. 2b). The submonthly covariance component also contributes slightly.

Next we examine the respective contributions from each Arctic Ocean gateway. The increase in ensemble mean Eulerian-mean OHT into the Arctic is primarily due to a strengthening of the OHT through the BSO, which provides 41% of the total Eulerian-mean OHT increase between 1961–80 and 2081–2100

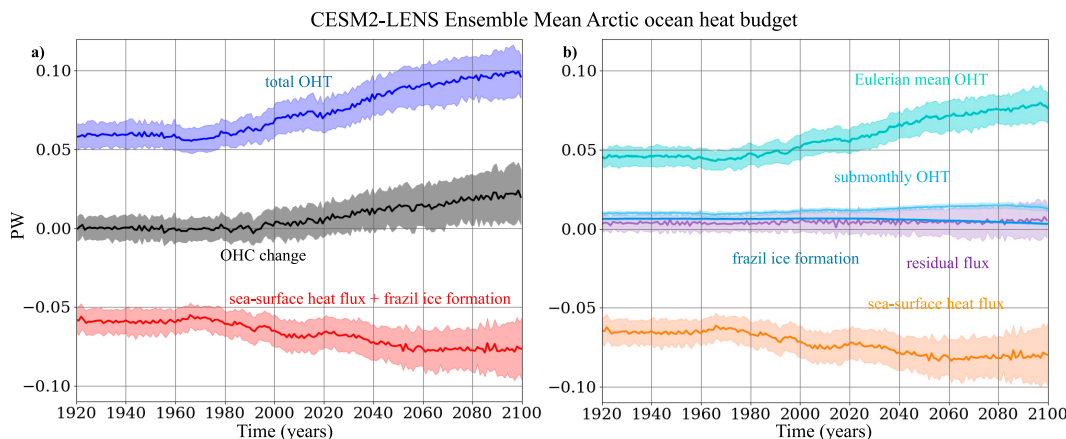


FIG. 2. (a) Ocean heat budget for the Arctic Ocean, bounded by the five Atlantic–Pacific Arctic gateways (see Fig. 1). Positive values indicate ocean heat gain, and negative values indicate ocean heat loss. The blue line represents the total OHT into the Arctic, the red line represents the net sea surface heat flux into the Arctic Ocean (including the heat flux due to frazil ice formation), and the black line represents the net ocean heat content change. The OHT plotted here includes the parameterized bolus and diffusive components approximated as explained in Eq. (4). (b) Decomposition of heat budget components. The cyan line represents the Eulerian mean OHT, aqua represents the submonthly OHT, teal represents the ocean heat gain resulting from frazil ice formation, orange represents the net sea surface heat flux (including both the atmosphere–ocean and ice–ocean heat fluxes), and purple represents the residual between the ocean heat content change computed explicitly [black line in (a)] and the sum of the other components plotted here, which is interpreted as the missing parameterized bolus and diffusive OHT. Lines represent ensemble means and shading represents one standard deviation across ensemble members.

(Fig. 3b). However, both the Fram and Bering Straits also experience large increases in OHT. After remaining approximately constant, OHT through the Fram Strait decreases in 1980–2000 before steadily increasing through 2100, starting from 0.01 PW over 2000–20 and reaching 0.02 PW by 2081–2100. In the Bering Strait, the OHT is very small during most of the twentieth century, but strengthens steadily after 1970, increasing to over 0.01 PW by 2081–2100 (Fig. 3b). Note that the volume transport across the Bering Strait actually declines slightly during the twenty-first century (Fig. 3a). The Nares Strait OHT changes very little until about 2040, when it starts to decrease (Fig. 3b). This is partially due to a decrease in southward volume transport over the same period (Fig. 3a). The Barrow Strait does not contribute significantly to the net OHT into the Arctic, and weakens slightly over time as the volume transport decreases in magnitude (Figs. 3a,b).

Though the submonthly OHT is much smaller than the Eulerian mean, it still contributes between 14% and 18% of the total OHT (Fig. 3c), with that percentage decreasing over the course of the SSP3-7.0 period (2015–2100). The net submonthly OHT starts increasing at around 1965. After that, it increases from 0.009 PW over years 1961–80 to 0.014 PW by 2081–2100. These changes are dominated by changes in the submonthly OHT through the BSO and Bering Strait. The BSO contributes about 0.003 PW to this increase, while the Bering Strait submonthly OHT accounts for 0.002 PW (Fig. 3c). The increase in the Bering Strait can partially be explained by an increase in the submonthly transient kinetic energy there (not shown).

The volume transport changes do not seem to explain the BSO and Bering Strait OHT changes (Fig. 3a), two of the main contributors to the total OHT increase. However,

the increased OHT across the Fram Strait from 2020 to 2075 can be partially explained by changes in the volume transport there. Interestingly, there appears to be an anticorrelation between the Fram Strait and Nares Strait volume transports, with the large changes in the two toward the end of the simulations nearly compensating each other (Fig. 3a). This feature will be revisited in the discussion section.

To provide a more quantitative understanding regarding how much of the OHT changes is due to the changes in the volume transport versus temperature, we decompose the Eulerian mean OHT anomalies into contributions from “dynamic” changes in circulation, “thermodynamic” temperature changes, and a “nonlinear” term, which represents anomalies due to concurrent changes in temperature and velocity. Though this separation is somewhat arbitrary as velocity and temperature changes are intrinsically linked via geostrophy, it is still useful. This method is outlined in Oldenburg et al. (2018) among others:

$$\begin{aligned} \text{OHT}'(t) = & \underbrace{\rho c_p \int_{x_1}^{x_2} \int_{z_{\text{bot}}}^0 \langle v \rangle (\dot{\theta} - \dot{\theta}_{\text{ref}}) dz dx}_{\text{thermodynamic}} \\ & + \underbrace{\rho c_p \int_{x_1}^{x_2} \int_{z_{\text{bot}}}^0 \dot{v} \langle \theta - \theta_{\text{ref}} \rangle dz dx}_{\text{dynamic}} \\ & + \underbrace{\rho c_p \int_{x_1}^{x_2} \int_{z_{\text{bot}}}^0 \dot{v} (\dot{\theta} - \dot{\theta}_{\text{ref}}) dz dx}_{\text{nonlinear}}, \end{aligned} \quad (6)$$

where angle brackets represent a time mean of a given variable (i.e., $\langle v \rangle$ and $\langle \theta \rangle$), and dots represent temporal anomalies

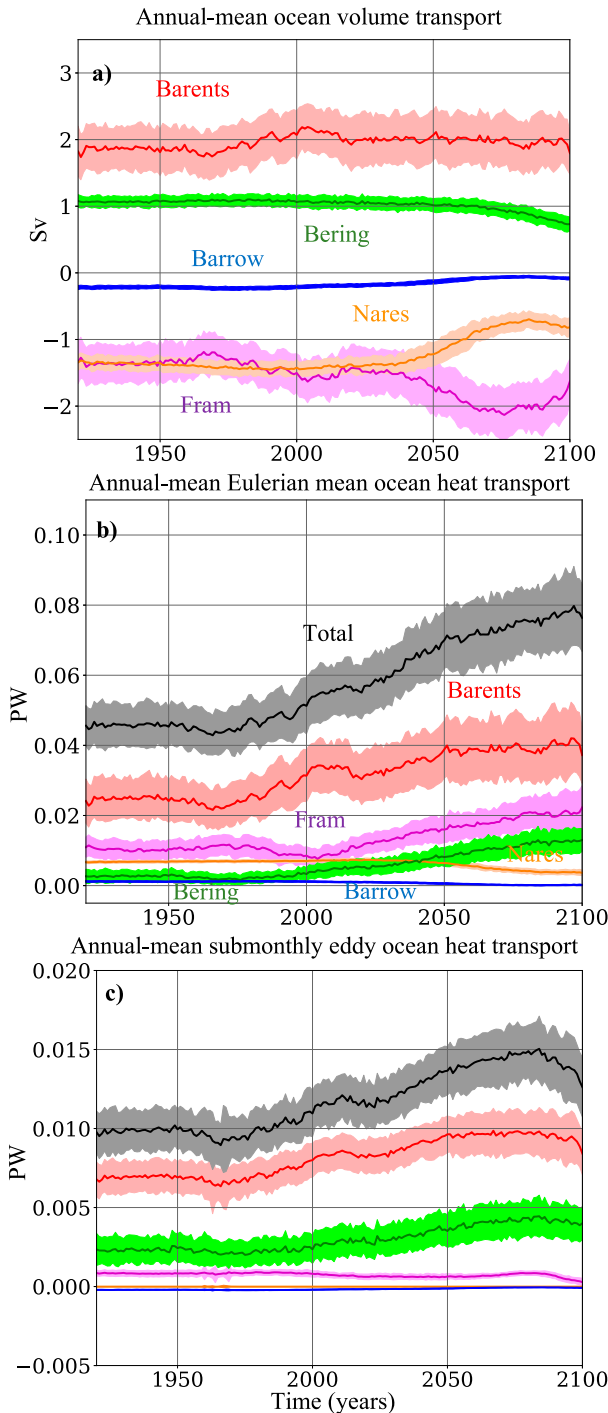


FIG. 3. (a) Annual-mean volume transport (for the liquid water only) through the Arctic gateways. (b) Annual-mean Eulerian-mean OHT across the Arctic gateways. (c) Annual-mean submonthly OHT across the Arctic gateways. Lines represent ensemble means and shading represents one standard deviation across ensemble members.

of a variable relative to its time mean (i.e., \bar{v} and $\bar{\theta}$). For the time-mean temperatures and velocities in Eq. (6), we use the period 1920–80, during which there is very little change in the ensemble mean ocean heat budget (Fig. 2).

Here, instead of simply using 0°C as our OHT reference temperature, we reference OHT to the spatially averaged time-varying Arctic Ocean temperature. Though this does not substantially influence the partitioning of the net OHT through the Arctic gateways, Eq. (6) is more sensitive to the reference temperature. This is because the thermodynamic and nonlinear terms are calculated using temperature anomalies rather than full temperatures.

The net OHT increase into the Arctic is largely driven by thermodynamic (temperature) changes, but the nonlinear components also play a major role, while the dynamic components partially compensate during the last 50 years (Fig. 4a). Thermodynamic changes contribute 0.03 PW to the net OHT increase from 1920–80 to 2081–2100, while nonlinear changes contribute 0.01 PW. Dynamic circulation changes, on the other hand, act to decrease the net OHT after 2040, with an anomaly slightly smaller than -0.01 PW over the same period due to negative dynamic components from the Nares and Barrow Straits (not shown). BSO and Bering Strait OHT changes are primarily driven by thermodynamic changes (Figs. 4c,d). In the Bering Strait, the nonlinear term acts to weaken the OHT (Fig. 4d). In the Fram Strait, the thermodynamic and dynamic components contribute very little to the OHT anomaly, which is driven almost entirely by nonlinear changes (Fig. 4b).

To further investigate the nonlinear component of the Fram Strait OHT, we also decompose this OHT into baroclinic and barotropic terms using the depth-mean velocity and temperature:

$$\text{OHT}'(t) = \underbrace{\rho c_p \int_{x_1}^{x_2} \int_{z_{\text{bot}}}^0 \underline{v}(\underline{\theta} - \theta_{\text{ref}}) dz dx}_{\text{barotropic}} + \underbrace{\rho c_p \int_{x_1}^{x_2} \int_{z_{\text{bot}}}^0 v_*(\theta_* - \theta_{\text{ref}}) dz dx}_{\text{baroclinic}}, \quad (7)$$

where the underline represents depth-mean values, and the subscript * represents anomalies relative to the depth means.

This nonlinear component of the Fram Strait OHT is driven by baroclinic changes rather than barotropic changes (Fig. 5a), i.e., changes in the vertical structure of the velocity and temperature. More specifically, the middle and deep layers of the Fram Strait cool while the upper layer warms relative to the vertically averaged values, which indicates an increase in stratification between the layers. There is a dramatic increase in the southward flow in the middle depths of the Fram Strait, while the upper and deep areas of the strait exhibit anomalous northward flow (Fig. 5b).

b. Variability and background seasonality of sea surface heat flux components

Here, we adhere to the ocean heat budget perspective, i.e., ocean model output is used for all the surface flux components from the atmosphere and sea ice.

Before investigating how much the sea surface flux components change over time, we first look at their background seasonality in the 1920–40 period. This will help us understand the times of year when different sea surface heat flux components are important. In late spring and summer, the ocean

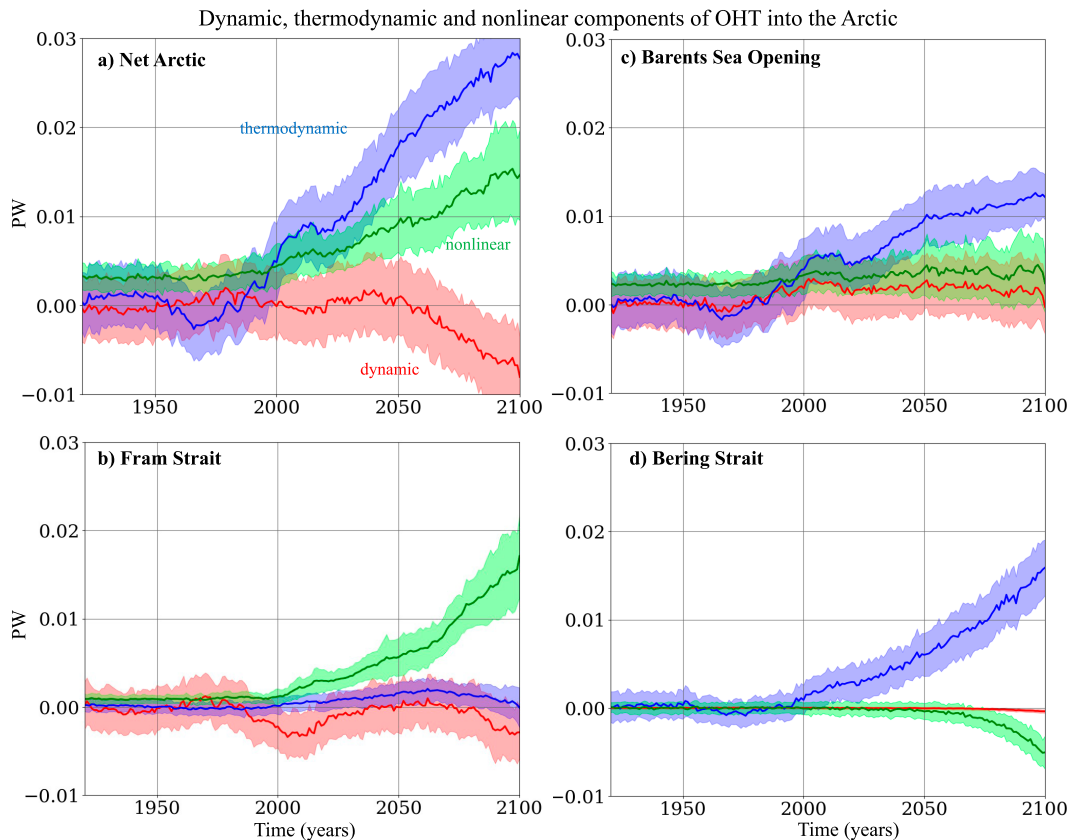


FIG. 4. Thermodynamic (blue), dynamic (red), and nonlinear (green) components of OHT anomalies relative to 1920–80 for (a) net OHT, (b) Fram Strait OHT, (c) Barents Sea Opening OHT, and (d) Bering Strait OHT. Lines represent ensemble means and shading represents one standard deviation across ensemble members.

experiences a net gain of heat (Fig. 6a, gray line) from the atmosphere due to strong shortwave radiation (Fig. 6b, orange line). Meanwhile, heat is lost to sea ice due to ice melt (Figs. 6a,b, blue lines). In autumn and winter (October–March),

the ocean loses heat to both the atmosphere and ice, but primarily to the atmosphere as heat gained via shortwave radiation in summer is then lost via longwave radiation, latent and sensible heat fluxes (Figs. 6a,b). After October, rapid sea ice expansion

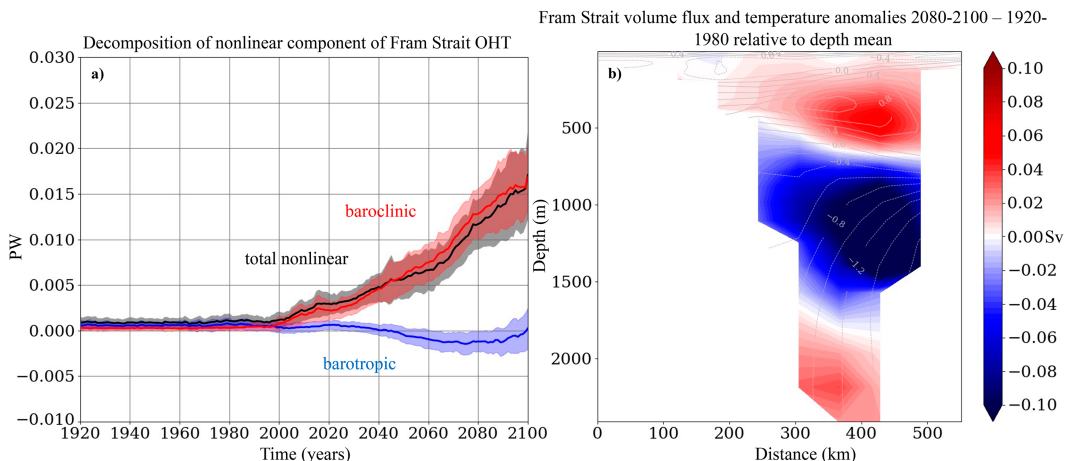


FIG. 5. (a) Barotropic (blue) and baroclinic (red) contributions to the nonlinear component (black) of the Fram Strait OHT. Lines represent ensemble means and shading represents one standard deviation across ensemble members. (b) Fram Strait volume flux (Sv) and temperature ($^{\circ}\text{C}$) anomalies relative to depth means for 2080–2100 relative to 1920–80.

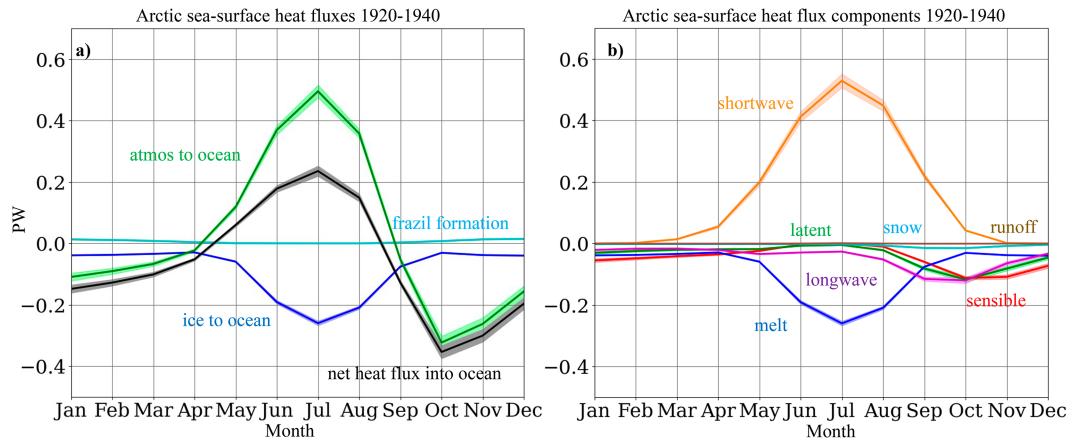


FIG. 6. (a) Seasonality of Arctic ocean heat exchanges with the atmosphere (green) and sea ice (blue) averaged over years 1920–40. (b) Seasonality of Arctic sea surface heat flux components. Lines represent ensemble means and shading represents one standard deviation across ensemble members. The positive values indicate heat gain by the ocean. Note that the heat exchanges are expressed in PW after an area integration over the Arctic domain.

reduces the ocean's exposure to the atmosphere and hence reduces its heat loss to the atmosphere. The ocean gains a minimal amount of heat via frazil ice formation from October through March (Fig. 6a).

Next, we examine the long-term changes of the sea surface heat fluxes. Throughout the period, the ocean loses heat through the sea surface, with enhanced surface heat loss after 1980 (black line in Fig. 7a, and also Fig. 2a), in response to the increased OHT into the Arctic as discussed in section 3a. The ocean primarily loses heat to the sea ice (blue line in Fig. 7a), but is slightly offset by the ocean heat gain from the atmosphere until around 2050 (green line in Fig. 7a). Afterward the ocean begins to experience net heat loss to the atmosphere. The ocean starts to lose less heat to the ice beginning ~2030 due to reduced sea ice cover and an associated reduction in heat fluxes needed for melting (Figs. 1c and 7b).

However, the heat loss to the atmosphere after 2050 overcompensates the reduced heat loss to the ice, so that the total heat loss continues to increase. Essentially, the heat transported into the Arctic Ocean via OHT is primarily used to melt the sea ice until the sea ice coverage declines substantially in the mid-21st century and the exposed ocean surface increases, after which heat begins to flux out to the atmosphere. In terms of heat flux components, absorbed shortwave radiation strengthens due to decreasing surface albedo with more open ocean as well as reduced cloud cover (Figs. 8a,b). However, starting in 2040, this increased heat flux is compensated by strengthened upwelling longwave radiation as well as stronger sensible and latent heat loss reflecting ocean warming and more extended open waters (Fig. 7b). Though the downwelling longwave radiation also increases over the course of the simulations, this increase is compensated by the increasing

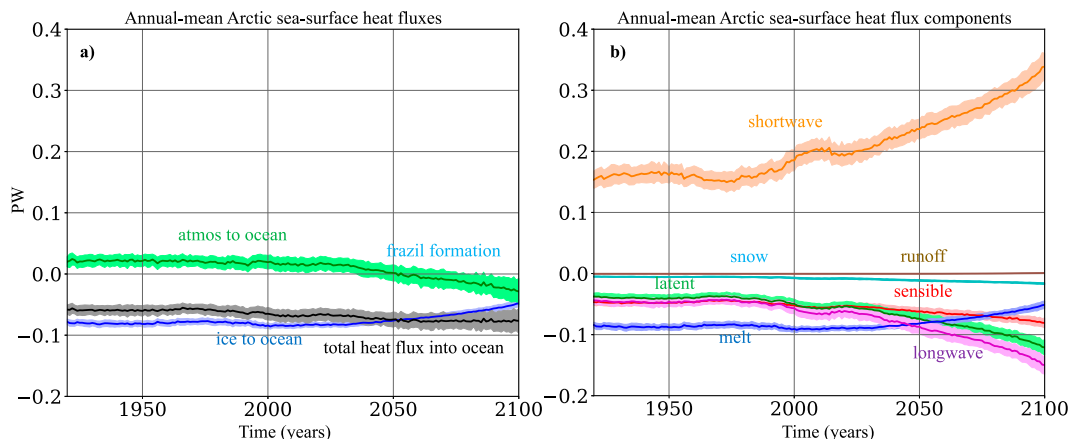


FIG. 7. Time series of ensemble mean annual-mean Arctic (a) total air-sea and ocean-ice heat fluxes and (b) sea surface heat flux components. Shading represents one standard deviation across ensemble members. The positive values indicate heat gain by the ocean. Note that the heat exchanges are expressed in PW after an area integration over the Arctic domain.

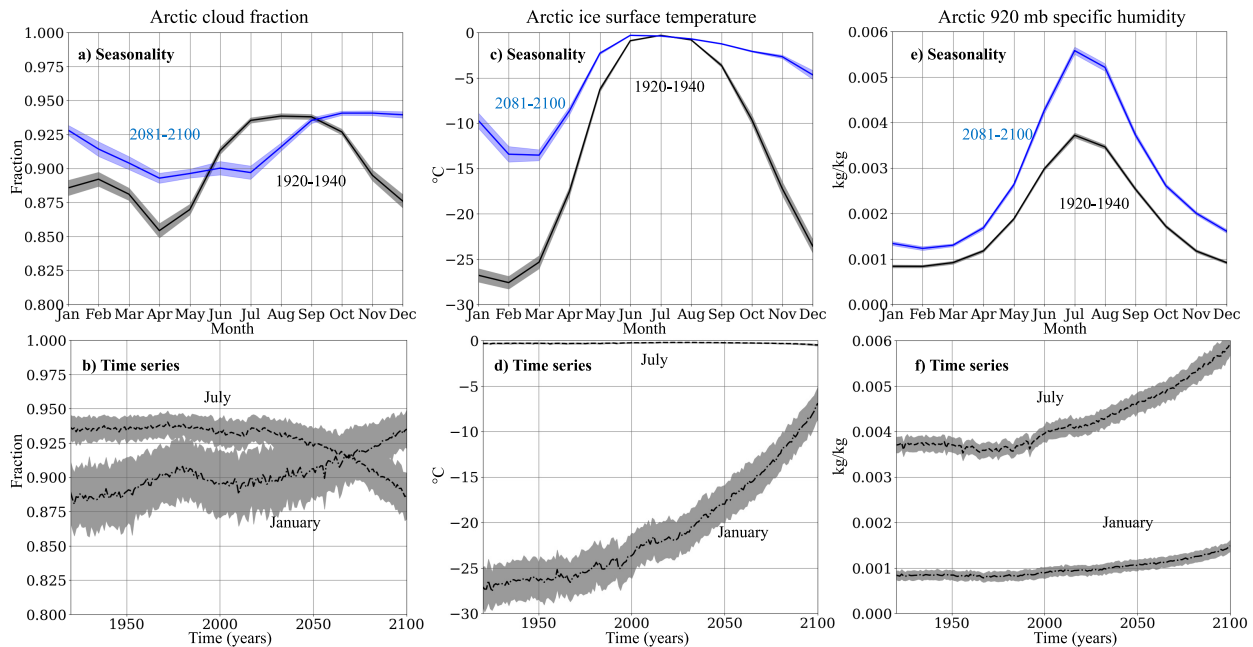


FIG. 8. (a) Mean seasonality for two different periods and (b) January and July time series for the cloud fraction over areas north of 68°N . (c),(d) As in (a) and (b), but for Arctic sea ice surface temperature. (e),(f) As in (a) and (b), but for specific humidity at 920 hPa over areas north of 68°N .

upwelling longwave radiation (Fig. 9b), which is consistent with the balance in the mean seasonal cycle (Fig. 9a) and explains the increased ocean cooling due to longwave radiation out to 2100 (Fig. 7b).

4. Arctic sea ice heat budget

The Arctic sea ice heat budget is defined as

$$\frac{d}{dt}\text{HC} = F_{\text{ocn}} + F_{\text{atm}} + F_{\text{residual}}, \quad (8)$$

where HC refers to the heat content of the snow and ice, F_{ocn} is the ocean–ice heat flux, F_{atm} is the atmosphere–ice flux, and F_{residual} is the residual term between $(d/dt)\text{HC}$ and the two other terms, which represents the contribution from ice export through the Fram Strait as well as any error introduced by the usage of monthly mean data for our heat budget calculation.

The atmosphere–ice flux F_{atm} can be split into components:

$$F_{\text{atm}} = F_{\text{SW}} + F_{\text{sensible}} + F_{\text{latent}} + F_{\text{LW}}, \quad (9)$$

where F_{SW} is the net absorbed shortwave radiation, i.e., the incident shortwave radiative flux minus the reflected and transmitted shortwave radiation, F_{sensible} is the sensible heat flux, F_{latent} is the latent heat flux, and F_{LW} is the net longwave radiative flux.

Over years 1920–40, the Arctic is almost entirely ice-covered in March, aside from the southern section of the Barents Sea (contours in Fig. 1a). In September, much of the Arctic remains at least partially ice-covered, aside from

the southernmost regions (contours in Fig. 1b). Ensemble mean September sea ice concentration starts to decrease rapidly around 1980 with a brief slowdown during 2010–20 (Fig. 1c). The Arctic becomes virtually ice-free (defined as below 1 million km^2 coverage) in September by 2035. In March, sea ice extent starts decreasing also around 1980, with the rate of decline increasing over time, especially for the last 20 years (Fig. 1c). Unlike in September, where sea ice decline happens across the entire Arctic, March sea ice decline occurs almost entirely in the southernmost areas, namely, the Barents, Kara, Iceland, and Greenland Seas as well as the Chukchi and Beaufort Seas on the Pacific side (Fig. 1a). This is unsurprising considering the large increases in OHT across the shallow Bering Strait and BSO (Fig. 3b).

To understand how much heat from the ocean and atmosphere goes toward melting Arctic sea ice, we analyze atmosphere–ice and ocean–ice heat fluxes using the model output variables from the sea ice model component. We use Arctic heat fluxes in watts per square meter (W m^{-2}) rather than total Arctic integrated fluxes in petawatts (PW). We do this because the magnitudes of the Arctic integrated fluxes in petawatts are closely tied to the amount of ice present, and hence it is difficult to determine whether changes in these fluxes are due to sea ice loss or other factors. Arctic heat fluxes per unit area, on the other hand, will only vary due to changes in ocean–ice–atmosphere interactions, and not due to reductions in sea ice area.

We first look at the background seasonality (from 1920 to 1940) of these heat fluxes to ascertain what drives the seasonal cycle of sea ice (Fig. 10). In autumn and winter (October–April), the sea ice gains a small amount of heat from the

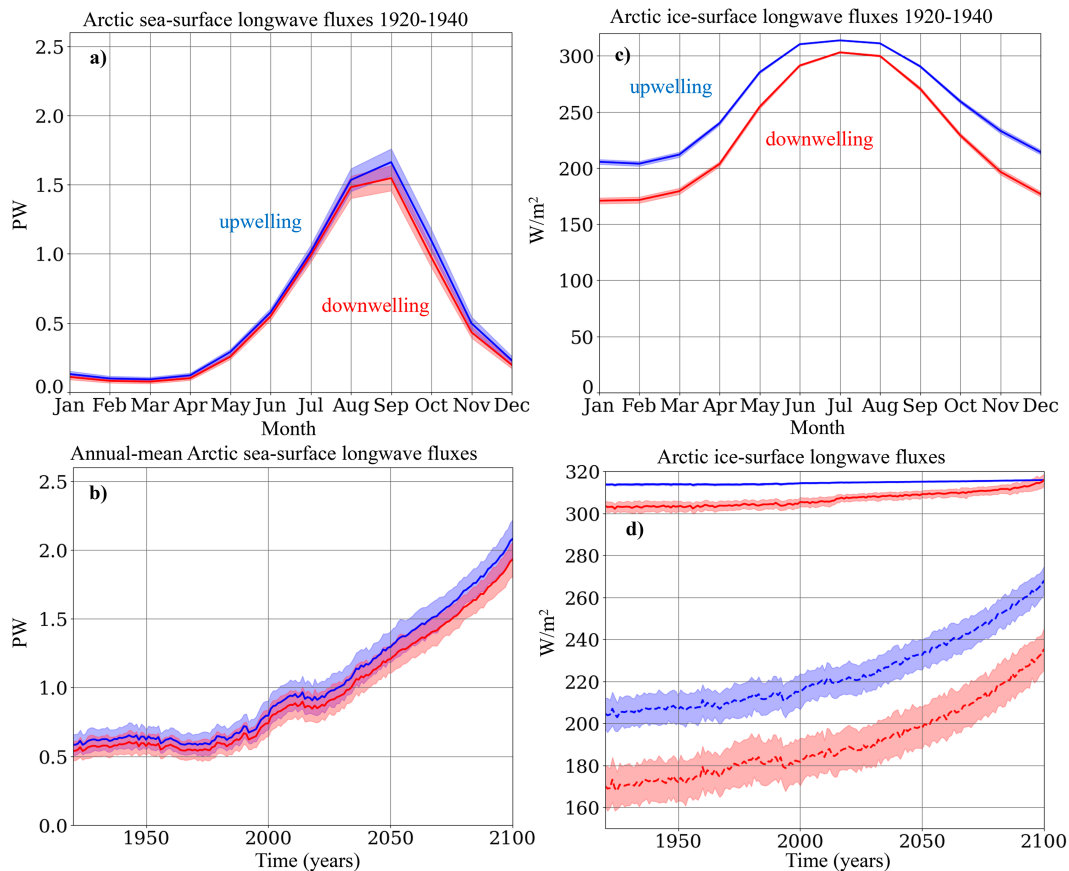


FIG. 9. (a) Seasonality of upwelling (blue) and downwelling (red) longwave radiation flux magnitudes over ice-free areas of the Arctic for the background climate in 1920–40. The signs of the upwelling radiation fluxes are reversed to simplify comparisons. Ice-free areas are determined by using ocean model output. (b) Time series of annual-mean longwave radiation fluxes over ice-free areas of the Arctic. (c) Seasonality of longwave radiation fluxes over ice-covered areas of the Arctic in 1920–40. (d) Time series of January-mean (dashed lines) and July-mean (solid lines) longwave radiation fluxes over ice-covered areas of the Arctic. Ice-covered areas include only ice-covered portions of each grid cell, as determined from ice model output. Lines represent ensemble means and shading represents one standard deviation across ensemble members. Note that (a) and (b) are expressed in PW (i.e., area integrated) to be consistent with Figs. 5 and 6, while (c) and (d) are plotted in W m^{-2} .

ocean while losing large amounts of heat to the atmosphere (Fig. 10a) due to upwelling longwave radiation and the minimal incoming shortwave radiation during those months (Fig. 10b). This heat loss drives seasonal ice growth and cooling during that period. In late spring and summer, the sea ice gains substantial heat from both the ocean and atmosphere. In June and July, the atmosphere is the dominant heat source due to strong shortwave radiation (Fig. 10b), but in August and September, the ocean becomes the primary source of heat for the ice (Fig. 10a).

When analyzing the winter and summer Arctic sea ice heat budgets, we focus on heat fluxes during January and July rather than March and September. We do this because sea ice growth and melting are more concentrated during the peaks of winter and summer than in March and September, when ocean–ice–atmosphere heat fluxes are small.

During the historical and SSP3-70 period, in January there is relatively little change in the ocean–ice heat flux but for a slight increase over time (Fig. 11a). Meanwhile, ice heat loss to the atmosphere increases as a result of increased latent and sensible heat loss (Figs. 11a,c). The latent and sensible heat fluxes increase as a result of a greatly enhanced snow/ice surface temperature (Figs. 8c,d), which increases the temperature gradient between the winter atmosphere and snow/ice surface. In July, the atmosphere is initially the primary source of heat due to the strong shortwave radiation, accounting for 55% of the total heat flux into the sea ice over years 1920–40. However, the ocean–ice heat flux slowly increases and becomes the more dominant source of heat for the ice by 2020 (Fig. 11b). The ocean–ice heat flux then increases exponentially in the final decades of the simulations as Arctic sea ice concentration approaches zero. On the other hand, the atmosphere–ice heat flux only slightly increases over time as the downwelling longwave

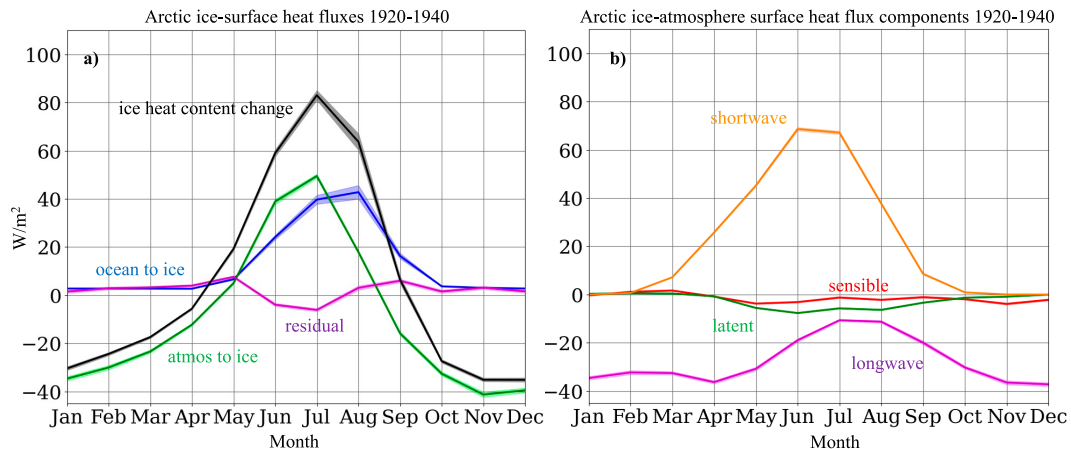


FIG. 10. (a) Mean seasonality of Arctic sea ice heat gain from the atmosphere (green) and the ocean (blue), respectively, in 1920–40. The residual (purple line) represents the difference between the ice heat content change and the sum of the other terms. (b) Mean seasonality of Arctic atmosphere–ice heat flux components. The shortwave radiation here includes only that which is absorbed by the ice. Positive values indicate ice heat gain. Lines represent ensemble means and shading represents one standard deviation across ensemble members.

radiation and sensible heat flux increase, though this is partially counteracted by a reduction in the absorbed shortwave radiation resulting from increased transmission to the ocean layer below (Fig. 11d), which occurs due to thinning sea ice. The shift of

the primary heat source for the sea ice from atmosphere to ocean is also present when looking at Arctic integrated heat fluxes in PW (not shown), and hence is not simply a result of vanishing sea ice concentration.

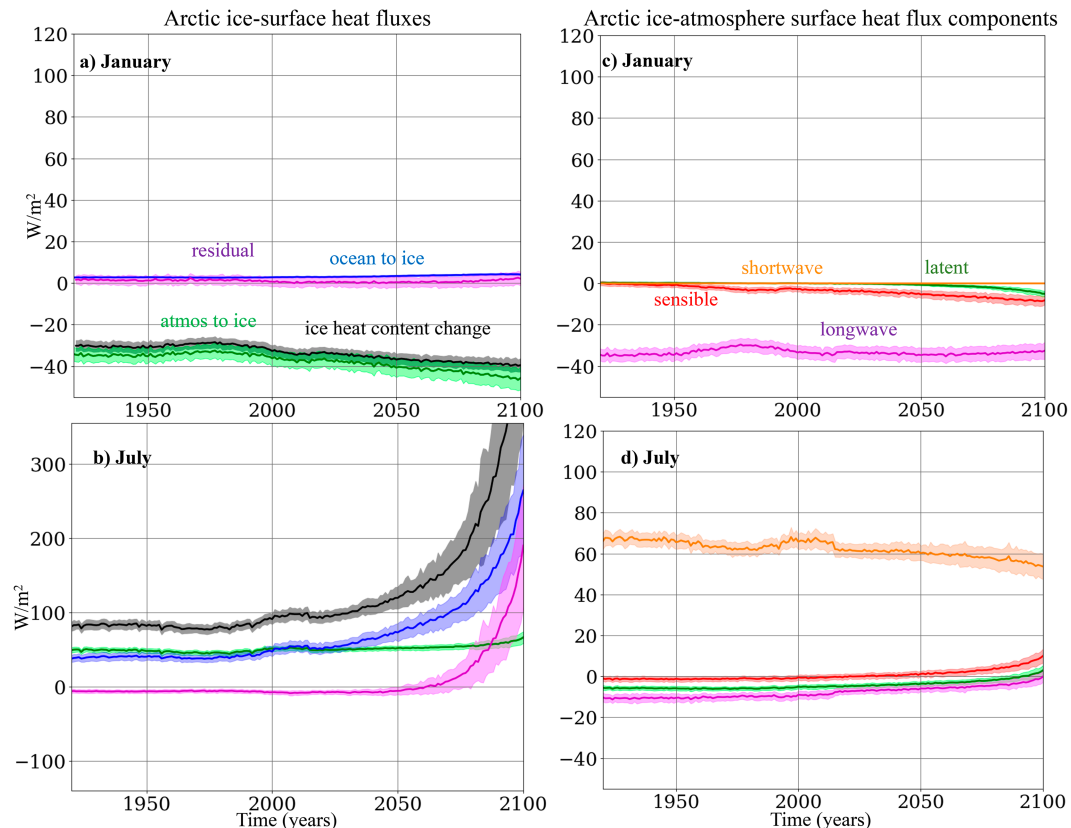


FIG. 11. Time series of (a) January-mean and (b) July-mean heat fluxes into sea ice. Time series of (c) January-mean and (d) July-mean Arctic atmosphere–ice heat flux components. Positive values indicate ice heat gain. Lines represent ensemble means and shading represents one standard deviation across ensemble members.

Analysis of upwelling and downwelling longwave radiation fluxes

Finally, we analyze the downwelling and upwelling longwave radiation fluxes separately to understand why the net longwave fluxes change the way they do, because the longwave is an important driver for the increase in the atmosphere–ice heat flux in summer (Figs. 9b,d). Both the upwelling and downwelling longwave fluxes are stronger in summer than in winter (Fig. 9c), as expected given that both the ice and atmosphere are warmer in summer. However, the downwelling radiation increases more than the upwelling component seasonally, leading to a smaller net longwave radiation flux in summer (Fig. 9c). In January, both the downwelling and upwelling longwave radiation fluxes increase substantially as the Arctic warms. However, these changes more or less cancel each other out (Fig. 9d), leading to little change in the net longwave flux (Fig. 10c). In July, on the other hand, upwelling longwave radiation changes very little, while the downwelling longwave radiation increases enough to overwhelm the upwelling flux by the end of the simulations (Figs. 9e and 10d).

Different factors within the Arctic may impact longwave fluxes, i.e., the cloud fraction, ice surface temperature, and specific humidity. Given that the cloud fraction and specific humidity are calculated by the atmospheric model, which has a different grid than the ocean and ice models, we simply average these quantities north of 68°N. Over the course of the simulations, cloud cover during autumn, winter and spring months increases substantially, which contributes to the enhanced downwelling longwave radiation in January (Figs. 8a,b and 9d), in line with observations (Previdi et al. 2021), given the impact of clouds on emissivity of the Arctic lower troposphere (Previdi et al. 2021). This results from enhanced ocean exposure to the atmosphere driving more evaporation, allowing for more cloud formation. The specific humidity increases throughout the year, which drives increased downwelling longwave radiation (Fig. 8f), given the impact of increased moisture content on atmospheric emissivity. In summer, this counteracts the reduced cloud cover, which does not increase alongside humidity due to a stable atmospheric boundary layer (Morrison et al. 2019).

The sea ice surface temperature in winter changes dramatically over the course of the simulations (Figs. 8c,d), with an increase from -26.8° to -9.8°C in January between years 1920–40 and years 2081–2100. This can explain the increase in upwelling longwave radiation, given that warmer surfaces emit more radiation. There is very little change in ice temperature in summer, when ice temperatures are already very close to the melting point in 1920–40 (Figs. 8c,d).

5. Discussion and conclusions

In this analysis, we have used a 100-member single-model large ensemble, which has given us the ability to separate forced variations from internal variability, and hence has allowed us to robustly project how the Arctic Ocean heat content tendency, OHT through the Arctic gateways, and sea surface heat fluxes change as a result of anthropogenic

forcing. Looking at the heat budgets for both the Arctic Ocean and sea ice separately has allowed us to quantify what drives sea ice heat gain and ocean surface heat loss.

Our results based on CESM2-LENS indicate an essential role for ocean heat transport in driving Arctic Ocean warming, in line with previous studies (Koenig and Brodeau 2014; Nummelin et al. 2017; Auclair and Tremblay 2018; Shu et al. 2022). In particular, we find that enhanced OHT through the BSO, Fram and Bering Straits all contribute substantially to the increased OHT into the Arctic. The strengthened OHT across these sectors is primarily due to temperature changes rather than circulation changes, aside from the Fram Strait, where volume transport varies substantially and nonlinear changes play a more prominent role. The increased OHT into the Arctic overwhelms the increased heat loss at the sea surface, and hence approximately 56% of this excess heat still remains stored within the ocean itself, with the other 44% being released to the ice and atmosphere (Fig. 2a).

During the historical period, all of the sea surface heat loss from the Arctic Ocean is transferred to sea ice rather than to the atmosphere, which actually acts as a minor heat source for the ocean in the annual mean sense (Fig. 7a). However, over the course of the simulations, the atmosphere becomes a heat sink for the Arctic Ocean as Arctic sea ice concentration reduces and more ocean surface is exposed to the atmosphere, more than making up for the decreased heat loss to the ice. While the shortwave radiation absorbed by the ocean in summer increases substantially due to reduced albedo, this excess heat is subsequently lost during autumn and winter due to enhanced upwelling longwave radiation as well as sensible and latent heat fluxes. This aligns with previous work describing the driving mechanism of the ice–albedo feedback (e.g., Screen and Simmonds 2010; Stroeve and Notz 2018; Previdi et al. 2021). Specifically, the increased upwelling longwave radiation is primarily driven by increased ocean temperature and more ocean exposure to the atmosphere.

This can also be viewed from the atmosphere's perspective (Fig. 12). Throughout the simulations, the ice acts as a heat source for the atmosphere in the annual-mean sense. As the sea ice declines over time, the atmospheric heat gain also decreases (Fig. 12a). Meanwhile, the ocean initially acts as a heat sink for the atmosphere. However, over time, as the ocean's exposure to the atmosphere increases, the ocean becomes a net source of heat for the atmosphere, and in turn compensates for the reduction in ice–atmosphere heat fluxes. As a result, unlike the net heat fluxes into the ocean and ice, the annual-mean net heat flux into the atmosphere does not exhibit any significant trend (Fig. 12a). Interestingly, despite the fact that the annual-mean heat flux into the atmosphere remains unchanged throughout the simulations, the seasonality of this heat flux actually increases due to an enhanced seasonality of the ocean–atmosphere heat flux (Figs. 12b,c), likely due to more ocean exposure to the atmosphere. This more than compensates for the reduced seasonality of the ice–atmosphere heat flux (Fig. 12d).

In summer, sea ice loss occurs throughout the Arctic, which becomes almost entirely ice-free in September by 2035. In winter, sea ice decline happens much more gradually and

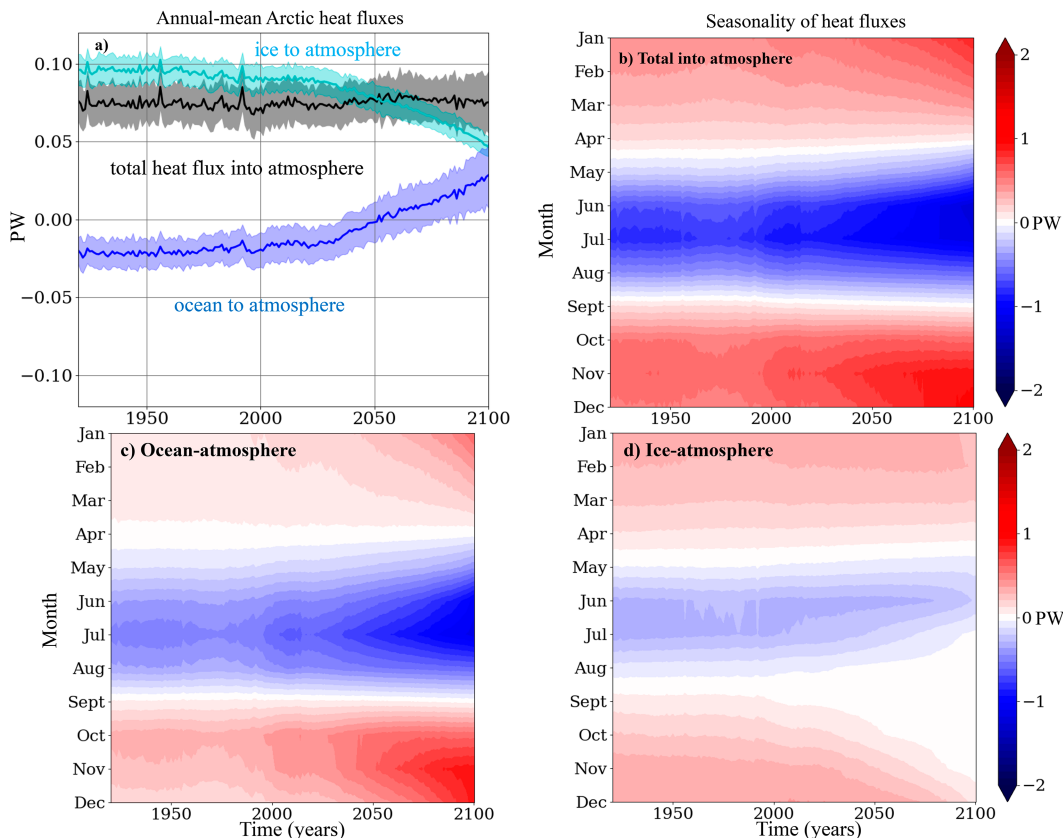


FIG. 12. (a) Time series of annual-mean Arctic ocean–atmosphere (purple) and sea ice–atmosphere (turquoise) heat fluxes. Lines represent ensemble means and shading represents one standard deviation across ensemble members. Positive values indicate atmospheric heat gain. Time evolution of the seasonality of (b) total, (c) ocean–atmosphere and (d) ice–atmosphere heat fluxes.

occurs predominantly in the Barents Sea, though there is some ice loss in the Chukchi and Beaufort Seas as well. This is in agreement with recent observational studies of winter Arctic sea ice loss (Onarheim et al. 2018), though there are indications that the recent winter ice loss may have been mainly due to natural variability (Yeager et al. 2015; Li et al. 2017).

The atmosphere and ocean are comparable sources of heat for the ice in summer. The atmosphere dominates in early and midsummer due to shortwave radiation while the ocean is the primary heat source in August and September as the ocean reaches its peak seasonal temperature and shortwave radiation weakens. In winter, the ocean provides a minimal amount of heat to the ice, while the ice loses substantial heat to the atmosphere as ice growth and cooling occur. Heat loss to the atmosphere increases over time due to strengthened sensible and latent heat loss. In summer, as sea ice loss accelerates over the course of the simulations, the ocean starts to become the dominant heat source for the ice, and then the ocean–ice heat flux grows exponentially as the ice disappears. This likely occurs due to a large increase in absorbed shortwave radiation in formerly predominantly ice-covered areas (cf. Timmermans 2015), which drives upper ocean warming and increased stratification, greatly enhancing the ocean–ice

heat flux. Given this effect, it is difficult to determine exactly how much of this ocean–ice flux is actually due to the enhanced OHT and how much is simply a result of a local feedback.

Downwelling longwave radiation to the ice increases in both summer and winter, in line with other modeling, observational and reanalysis-based studies which emphasize its role in Arctic Amplification and associated sea ice loss (Burt et al. 2016; Kim et al. 2016; Alexeev et al. 2017; Kim and Kim 2017; Kim et al. 2019). In summer, this is primarily driven by a substantial increase in specific humidity and a warmer atmosphere, which makes sense given the role of temperature and humidity in downwelling longwave radiation (e.g., Wild et al. 2001). Upwelling longwave radiation increases substantially in winter, primarily due to a dramatic increase in winter ice temperatures. Downwelling longwave radiation increases then largely because of a warmer atmosphere, increased humidity and enhanced cloud cover, which has been found to be a direct result of sea ice loss and increased ocean–atmosphere exposure (e.g., Kay and Gettelman 2009; Morrison et al. 2019; Previdi et al. 2021). Cloud cover in summer actually declines over time, and hence does not appear to be impacted by sea ice loss, in line with previous analyses (Kay and Gettelman 2009; Morrison et al. 2019; Previdi et al. 2021). This is because

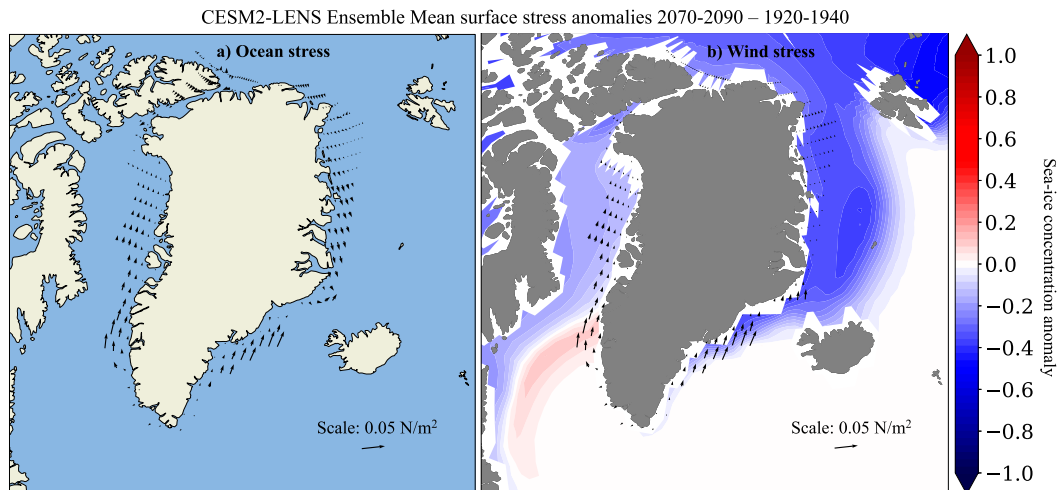


FIG. 13. Anomalies in (a) annual-mean surface stress felt by ocean (from ocean model output variables) and (b) annual-mean wind stress (from the atmospheric model output variables with reversed sign) and sea ice concentration (colors) over years 2070–90 relative to 1920–40. Years 2070–90 are chosen because the anomalies in the Fram and Nares Straits volume transports reach their maxima during that period.

the atmospheric boundary layer in summer is very stable due to a small air–sea temperature gradient, which is expected to remain in place in the future. Because of this stability, the surface has little impact on summer cloud cover (Morrison et al. 2019). As the Arctic atmosphere warms more rapidly than the ocean, this stability may even strengthen over time (Morrison et al. 2019), which would explain the reduced summer cloud cover. This decline in cloud cover cannot be explained by sea ice loss, because sea ice decline would act to increase cloud cover due to enhanced ocean exposure to the atmosphere.

There are a few caveats to this analysis. First, we only used one model, meaning that our results are very susceptible to systemic biases in the model. Second, the model used here has an ocean, ice and atmospheric horizontal resolution of 1° . Models with a 1° ocean resolution tend to underestimate Atlantic and Pacific OHT and misrepresent Arctic sea ice area and volume (Docquier et al. 2019). Representation of surface ocean properties is also greatly improved at higher resolutions (Docquier et al. 2019). Third, Arctic sea ice in CESM2 is biased compared to recent observations (Fig. 1c). Late summer sea ice concentration is lower than in present-day observations, which has been linked to the sea ice being too thin in winter (Danabasoglu et al. 2020; DeRepentigny et al. 2020; DuVivier et al. 2020). This likely leads to other biases in the time evolution of sea ice extent (DeRepentigny et al. 2020; Kay et al. 2022). More specifically, the thin bias likely leads to ice-free summers occurring sooner than otherwise, further accelerating shortwave-radiation driven surface ocean warming and hence further enhancing the ocean–ice and ocean–atmosphere heat fluxes as a result. Also, the net heat transport through the Fram Strait is significantly underestimated compared to observations (Table 3), though the presence of potentially large natural variability in observations makes it difficult to reliably compare model and observational transports over short periods.

Toward the end of the simulations, the Nares and Fram Straits appear to experience nearly compensating changes in volume transports, indicating a relationship between the two straits. The nearly compensating anomalies in their volume transports over years 2070–90 can be linked to an anomalous alongshore surface stress on the ocean off the coast of Greenland during that period (Fig. 13a). This surface stress pattern drives an anomalous alongshore geostrophic velocity in the same direction. On the western coast of Greenland, these alongshore surface ocean stress anomalies are caused by anomalies in northward wind stress (Fig. 13b). On the eastern coast, however, especially on the northern half, there is very little change in alongshore wind stress. Instead, a loss of sea ice (color shading in Fig. 13b) leads to increased transmission of the wind stress to the ocean surface, which enhances the surface stress felt by the ocean there (Figs. 13a,b). The enhanced alongshore ocean surface stress on both sides of Greenland drives an anomalous alongshore geostrophic velocity, leading to these changes in the Nares and Fram Strait volume transports.

Though we focused primarily on ensemble mean changes, it is interesting to note that standard deviations across ensemble members for the OHC tendency, total OHT and sea surface heat flux increase substantially over time (Fig. 2a). The OHC tendency standard deviation more than doubles, and the standard deviations of the other variables nearly double as well. This indicates an increase in Arctic intrinsic climate variability. The reason for these increased standard deviations, however, is unclear. There is a corresponding change in the standard deviation in the sea ice concentration, but not in the ice volume, whose standard deviation actually decreases over time (not shown), which is puzzling. In terms of the OHT, its standard deviation increase is linked to an increase in the standard deviations of its thermodynamic and nonlinear components (Fig. 4a), which can partially be explained by a higher standard deviation of the volume-mean temperatures in the Fram and Bering Straits (not shown).

While we have elucidated what drives Arctic Ocean warming and also the role of atmosphere and ocean surface heat fluxes in driving sea ice loss, it is not clear exactly where the additional ocean heat is stored. To understand which ocean layers take up this heat and how much is ventilated toward the surface, it would be useful to calculate the heat budget of separate Arctic Ocean layers. Additionally, it could be interesting to look at how this differs between the Atlantic and Pacific sectors to see the relative importance of the ocean heat transport in driving sea ice loss in the two sectors. This is impacted by model biases in Arctic Ocean stratification, which are significant.

This research highlights the importance of ocean heat transport in driving Arctic warming and sea ice decline. The excess heat transported by the ocean through the Arctic gateways acts as a major heat source for both the Arctic sea ice and the atmosphere, though a majority of it still remains stored within the ocean over time.

Acknowledgments. The authors are grateful for support from the National Science Foundation (NSF) through Grant OPP-2106190/2106228. This work is also supported by the NSF National Center for Atmospheric Research, which is a major facility sponsored by NSF under the Cooperative Agreement 1852977. We also acknowledge the Community Earth System Model version 2 Large Ensemble Project and supercomputing resources provided by the Institute for Basic Science Center for Climate Physics in South Korea (<https://doi.org/10.5194/esd-2021-50>). Python code for PyPAGO can be found at <https://pypago.nicolasbarrier.fr/>.

Data availability statement. Information about data accessibility for the CESM2 Large Ensemble Simulations used in this study can be found on the CESM2-LENS website: <https://www.cesm.ucar.edu/community-projects/lens2/data-sets>.

REFERENCES

- Alexeev, V. A., J. E. Walsh, V. V. Ivanov, V. A. Semenov, and A. V. Smirnov, 2017: Warming in the Nordic Seas, North Atlantic storms and thinning Arctic Sea ice. *Environ. Res. Lett.*, **12**, 084011, <https://doi.org/10.1088/1748-9326/aa7a1d>.
- Årthun, M., T. Eldevik, L. H. Smedsrud, Ø. Skagseth, and R. B. Ingvaldsen, 2012: Quantifying the influence of Atlantic heat on Barents Sea ice variability and retreat. *J. Climate*, **25**, 4736–4743, <https://doi.org/10.1175/JCLI-D-11-00466.1>.
- , —, and —, 2019: The role of Atlantic heat transport in future Arctic winter sea ice loss. *J. Climate*, **32**, 3327–3341, <https://doi.org/10.1175/JCLI-D-18-0750.1>.
- Asbjørnsen, H., M. Årthun, Ø. Skagseth, and T. Eldevik, 2020: Mechanisms underlying recent Arctic Atlantification. *Geophys. Res. Lett.*, **47**, e2020GL088036, <https://doi.org/10.1029/2020GL088036>.
- Auclair, G., and L. B. Tremblay, 2018: The role of ocean heat transport in rapid sea ice declines in the Community Earth System Model large ensemble. *J. Geophys. Res. Oceans*, **123**, 8941–8957, <https://doi.org/10.1029/2018JC014525>.
- Beszczynska-Möller, A., R. A. Woodgate, C. Lee, H. Melling, and M. Karcher, 2011: A synthesis of exchanges through the main oceanic gateways to the Arctic Ocean. *Oceanography*, **24** (3), 82–99, <https://doi.org/10.5670/oceanog.2011.59>.
- Blackport, R., J. Screen, K. van der Wiel, and R. Bintanja, 2019: Minimal influence of reduced Arctic Sea ice on coincident cold winters in mid-latitudes. *Nat. Climate Change*, **9**, 697–704, <https://doi.org/10.1038/s41558-019-0551-4>.
- Burt, M. A., D. A. Randall, and M. D. Branson, 2016: Dark warming. *J. Climate*, **29**, 705–719, <https://doi.org/10.1175/JCLI-D-15-0147.1>.
- Chemke, R., L. M. Polvani, J. E. Kay, and C. Orbe, 2021: Quantifying the role of ocean coupling in Arctic amplification and sea-ice loss over the 21st century. *npj Climate Atmos. Sci.*, **4**, 46, <https://doi.org/10.1038/s41612-021-00204-8>.
- Chylek, P., C. Folland, J. D. Klett, M. Wang, N. Hengartner, G. Lesins, and M. K. Dubey, 2022: Annual mean Arctic amplification 1970–2020: Observed and simulated by CMIP6 climate models. *Geophys. Res. Lett.*, **49**, e2022GL099371, <https://doi.org/10.1029/2022GL099371>.
- Danabasoglu, G., and Coauthors, 2020: The Community Earth System Model version 2 (CESM2). *J. Adv. Model. Earth Syst.*, **12**, e2019MS001916, <https://doi.org/10.1029/2019MS001916>.
- DeRepentigny, P., A. Jahn, M. M. Holland, and A. Smith, 2020: Arctic Sea ice in two configurations of the CESM2 during the 20th and 21st centuries. *J. Geophys. Res. Oceans*, **125**, e2020JC016133, <https://doi.org/10.1029/2020JC016133>.
- Deser, C., R. Knutti, S. Solomon, and A. S. Phillips, 2012: Communication of the role of natural variability in future North American climate. *Nat. Climate Change*, **2**, 775–779, <https://doi.org/10.1038/nclimate1562>.
- , and Coauthors, 2020: Insights from Earth system model initial-condition large ensembles and future prospects. *Nat. Climate Change*, **10**, 277–286, <https://doi.org/10.1038/s41558-020-0731-2>.
- Deshayes, J., R. Curry, and R. Msadek, 2014: CMIP5 model inter-comparison of freshwater budget and circulation in the North Atlantic. *J. Climate*, **27**, 3298–3317, <https://doi.org/10.1175/JCLI-D-12-00700.1>.
- Docquier, D., and Coauthors, 2019: Impact of model resolution on Arctic Sea ice and North Atlantic Ocean heat transport. *Climate Dyn.*, **53**, 4989–5017, <https://doi.org/10.1007/s00382-019-04840-y>.
- DuVivier, A. K., M. M. Holland, J. E. Kay, S. Tilmes, A. Gettelman, and D. A. Bailey, 2020: Arctic and Antarctic Sea ice mean state in the Community Earth System Model version 2 and the influence of atmospheric chemistry. *J. Geophys. Res. Oceans*, **125**, e2019JC015934, <https://doi.org/10.1029/2019JC015934>.
- Eyring, V., S. Bony, G. A. Meehl, C. A. Senior, B. Stevens, R. J. Stouffer, and K. E. Taylor, 2016: Overview of the Coupled Model Intercomparison Project Phase 6 (CMIP6) experimental design and organization. *Geosci. Model Dev.*, **9**, 1937–1958, <https://doi.org/10.5194/gmd-9-1937-2016>.
- Fahrback, E., 2006: ASOF-N: Arctic-subarctic ocean flux array for European climate: North. Final Report: 1 January 2003 to 31 March 2006, Alfred Wegener Institut für Polar- und Meeresforschung Tech. Rep., Contract EVK2-CT-2002-00139, 164 pp., <http://epic-reports.awi.de/2719/1/Fah2006h.pdf>.
- Fasullo, J. T., J.-F. Lamarque, C. Hannay, N. Rosenbloom, S. Tilmes, P. DeRepentigny, A. Jahn, and C. Deser, 2022: Spurious late historical-era warming in CESM2 driven by prescribed biomass burning emissions. *Geophys. Res. Lett.*, **49**, e2021GL097420, <https://doi.org/10.1029/2021GL097420>.
- Francis, J. A., S. J. Vavrus, and J. Cohen, 2017: Amplified Arctic warming and mid-latitude weather: New perspectives on

- emerging connections. *Wiley Interdiscip. Rev.: Climate Change*, **8**, e474, <https://doi.org/10.1002/wcc.474>.
- Fu, W., J. K. Moore, F. W. Primeau, K. Lindsay, and J. T. Randerson, 2020: A growing freshwater lens in the Arctic Ocean with sustained climate warming disrupts marine ecosystem function. *J. Geophys. Res.: Biogeosci.*, **125**, e2020JG005693, <https://doi.org/10.1029/2020JG005693>.
- Grémillet, D., and S. Descamps, 2023: Ecological impacts of climate change on Arctic marine megafauna. *Trends Ecol. Evol.*, **38**, 773–783, <https://doi.org/10.1016/j.tree.2023.04.002>.
- Gupta, A. S., L. C. Muir, J. N. Brown, S. J. Phipps, P. J. Durack, D. Monselesan, and S. E. Wijffels, 2012: Climate drift in the CMIP3 models. *J. Climate*, **25**, 4621–4640, <https://doi.org/10.1175/JCLI-D-11-00312.1>.
- Heuzé, C., H. Zanowski, S. Karam, and M. Muilwijk, 2023: The deep Arctic Ocean and Fram Strait in CMIP6 models. *J. Climate*, **36**, 2551–2584, <https://doi.org/10.1175/JCLI-D-22-0194.1>.
- Holland, M., and C. Bitz, 2003: Polar amplification of climate change in coupled models. *Climate Dyn.*, **21**, 221–232, <https://doi.org/10.1007/s00382-003-0332-6>.
- Honda, M., J. Inoue, and S. Yamane, 2009: Influence of low Arctic sea-ice minima on anomalously cold Eurasian winters. *Geophys. Res. Lett.*, **36**, L08707, <https://doi.org/10.1029/2008GL037079>.
- Hu, X., Y. Li, S. Yang, Y. Deng, and M. Cai, 2017: Process-based decomposition of the decadal climate difference between 2002–13 and 1984–95. *J. Climate*, **30**, 4373–4393, <https://doi.org/10.1175/JCLI-D-15-0742.1>.
- Huang, J., and Coauthors, 2017: Recently amplified Arctic warming has contributed to a continual global warming trend. *Nat. Climate Change*, **7**, 875–879, <https://doi.org/10.1038/s41558-017-0009-5>.
- Hwang, J., Y.-S. Choi, W. Kim, H. Su, and J. H. Jiang, 2018: Observational estimation of radiative feedback to surface air temperature over northern high latitudes. *Climate Dyn.*, **50**, 615–628, <https://doi.org/10.1007/s00382-017-3629-6>.
- Johannessen, O. M., and M. W. Miles, 2011: Critical vulnerabilities of marine and sea ice-based ecosystems in the high Arctic. *Reg. Environ. Change*, **11**, 239–248, <https://doi.org/10.1007/s10113-010-0186-5>.
- Kay, J. E., and A. Gettelman, 2009: Cloud influence on and response to seasonal Arctic Sea ice loss. *J. Geophys. Res.*, **114**, D18204, <https://doi.org/10.1029/2009JD011773>.
- , and Coauthors, 2022: Less surface sea ice melt in the CESM2 improves Arctic Sea ice simulation with minimal non-polar climate impacts. *J. Adv. Model. Earth Syst.*, **14**, e2021MS002679, <https://doi.org/10.1029/2021MS002679>.
- Kim, B.-M., S.-W. Son, S.-K. Min, J.-H. Jeong, S.-J. Kim, X. Zhang, T. Shim, and J.-H. Yoon, 2014: Weakening of the stratospheric polar vortex by Arctic sea-ice loss. *Nat. Commun.*, **5**, 4646, <https://doi.org/10.1038/ncomms5646>.
- Kim, H.-M., and B.-M. Kim, 2017: Relative contributions of atmospheric energy transport and sea ice loss to the recent warm Arctic winter. *J. Climate*, **30**, 7441–7450, <https://doi.org/10.1175/JCLI-D-17-0157.1>.
- Kim, K.-Y., B. D. Hamlington, H. Na, and J. Kim, 2016: Mechanism of seasonal Arctic Sea ice evolution and Arctic amplification. *Cryosphere*, **10**, 2191–2202, <https://doi.org/10.5194/tc-10-2191-2016>.
- , J.-Y. Kim, J. Kim, S. Yeo, H. Na, B. D. Hamlington, and R. R. Leben, 2019: Vertical feedback mechanism of winter Arctic amplification and sea ice loss. *Sci. Rep.*, **9**, 1184, <https://doi.org/10.1038/s41598-018-38109-x>.
- Koenigk, T., and L. Brodeau, 2014: Ocean heat transport into the Arctic in the twentieth and twenty-first century in EC-Earth. *Climate Dyn.*, **42**, 3101–3120, <https://doi.org/10.1007/s00382-013-1821-x>.
- Lee, T., I. Fukumori, and B. Tang, 2004: Temperature advection: Internal versus external processes. *J. Phys. Oceanogr.*, **34** (8), 1936–1944, [https://doi.org/10.1175/1520-0485\(2004\)034<1936:TAIVEP>2.0.CO;2](https://doi.org/10.1175/1520-0485(2004)034<1936:TAIVEP>2.0.CO;2).
- Li, D., R. Zhang, and T. R. Knutson, 2017: On the discrepancy between observed and CMIP5 multi-model simulated Barents Sea winter sea ice decline. *Nat. Commun.*, **8**, 14991, <https://doi.org/10.1038/ncomms14991>.
- Mahlstein, I., and R. Knutti, 2011: Ocean heat transport as a cause for model uncertainty in projected Arctic warming. *J. Climate*, **24**, 1451–1460, <https://doi.org/10.1175/2010JCLI3713.1>.
- Manabe, S., and R. J. Stouffer, 1980: Sensitivity of a global climate model to an increase of CO₂ concentration in the atmosphere. *J. Geophys. Res.*, **85**, 5529–5554, <https://doi.org/10.1029/JC085iC10p05529>.
- Marshall, J., J. R. Scott, K. C. Armour, J.-M. Campin, M. Kelley, and A. Romanou, 2014: The ocean's role in the transient response of climate to abrupt greenhouse gas forcing. *Climate Dyn.*, **44**, 2287–2299, <https://doi.org/10.1007/s00382-014-2308-0>.
- Mauritzen, C., and Coauthors, 2011: Closing the loop—Approaches to monitoring the state of the Arctic Mediterranean during the international polar year 2007–2008. *Prog. Oceanogr.*, **90**, 62–89, <https://doi.org/10.1016/j.pocean.2011.02.010>.
- Meier, W. N., F. Fetterer, A. K. Windnagel, and J. S. Stewart, 2021: NOAA/NSIDC climate data record of passive microwave sea ice concentration, version 4. National Snow and Ice Data Center, accessed 12 June 2023, <https://doi.org/10.7265/efmz-2t65>.
- Morrison, A. L., J. E. Kay, W. R. Frey, H. Chepfer, and R. Guzman, 2019: Cloud response to Arctic Sea ice loss and implications for future feedback in the CESM1 climate model. *J. Geophys. Res. Atmos.*, **124**, 1003–1020, <https://doi.org/10.1029/2018JD029142>.
- Muulwijk, M., L. H. Smedsrud, M. Ilicak, and H. Drange, 2018: Atlantic water heat transport variability in the 20th century Arctic Ocean from a global ocean model and observations. *J. Geophys. Res. Oceans*, **123**, 8159–8179, <https://doi.org/10.1029/2018JC014327>.
- Nummelin, A., C. Li, and P. J. Hezel, 2017: Connecting ocean heat transport changes from the midlatitudes to the Arctic Ocean. *Geophys. Res. Lett.*, **44**, 1899–1908, <https://doi.org/10.1002/2016GL071333>.
- Oldenburg, D., K. C. Armour, L. Thompson, and C. M. Bitz, 2018: Distinct mechanisms of ocean heat transport into the Arctic under internal variability and climate change. *Geophys. Res. Lett.*, **45**, 7692–7700, <https://doi.org/10.1029/2018GL078719>.
- Onarheim, I. H., and M. Årthun, 2017: Toward an ice-free Barents Sea. *Geophys. Res. Lett.*, **44**, 8387–8395, <https://doi.org/10.1002/2017GL074304>.
- , T. Eldevik, M. Årthun, R. B. Ingvaldsen, and L. H. Smedsrud, 2015: Skillful prediction of Barents Sea ice cover. *Geophys. Res. Lett.*, **42**, 5364–5371, <https://doi.org/10.1002/2015GL064359>.
- , —, L. H. Smedsrud, and J. C. Stroeve, 2018: Seasonal and regional manifestation of Arctic Sea ice loss. *J. Climate*, **31**, 4917–4932, <https://doi.org/10.1175/JCLI-D-17-0427.1>.
- Overland, J. E., and Coauthors, 2016: Nonlinear response of mid-latitude weather to the changing Arctic. *Nat. Climate Change*, **6**, 992–999, <https://doi.org/10.1038/nclimate3121>.
- Pithan, F., and T. Mauritsen, 2014: Arctic amplification dominated by temperature feedbacks in contemporary climate models. *Nat. Geosci.*, **7**, 181–184, <https://doi.org/10.1038/ngeo2071>.

- Polyakov, I. V., and Coauthors, 2017: Greater role for Atlantic inflows on sea-ice loss in the Eurasian Basin of the Arctic Ocean. *Science*, **356**, 285–291, <https://doi.org/10.1126/science.aai8204>.
- , and Coauthors, 2020: Borealization of the Arctic Ocean in response to anomalous advection from sub-Arctic seas. *Front. Mar. Sci.*, **7**, 491, <https://doi.org/10.3389/fmars.2020.00491>.
- Previdi, M., K. L. Smith, and L. M. Polvani, 2021: Arctic amplification of climate change: A review of underlying mechanisms. *Environ. Res. Lett.*, **16**, 093003, <https://doi.org/10.1088/1748-9326/ac1c29>.
- Rantanen, M., A. Y. Karpechko, A. Lipponen, K. Nordling, O. Hyvärinen, K. Ruosteenoja, T. Vihma, and A. Laaksonen, 2022: The Arctic has warmed nearly four times faster than the globe since 1979. *Commun. Earth Environ.*, **3**, 168, <https://doi.org/10.1038/s43247-022-00498-3>.
- Roach, A. T., K. Aagaard, C. H. Pease, S. A. Salo, T. Weingartner, V. Pavlov, and M. Kulakov, 1995: Direct measurements of transport and water properties through the Bering Strait. *J. Geophys. Res.*, **100**, 18443–18457, <https://doi.org/10.1029/95JC01673>.
- Rodgers, K. B., and Coauthors, 2021: Ubiquity of human-induced changes in climate variability. *Earth Syst. Dyn.*, **12**, 1393–1411, <https://doi.org/10.5194/esd-12-1393-2021>.
- Rudels, B., M. Korhonen, U. Schauer, S. Pisarev, B. Rabe, and A. Wisotzki, 2015: Circulation and transformation of Atlantic water in the Eurasian Basin and the contribution of the Fram Strait inflow branch to the Arctic Ocean heat budget. *Prog. Oceanogr.*, **132**, 128–152, <https://doi.org/10.1016/j.pcean.2014.04.003>.
- Schauer, U., A. Beszczynska-Möller, W. Walczowski, E. Fährbach, J. Piechura, and E. Hansen, 2008: Variation of measured heat flow through the Fram Strait between 1997 and 2006. *Arctic-Subarctic Ocean Fluxes*, R. R. Dickson, J. Meincke, and P. Rhines, Eds., Springer, 65–85, https://doi.org/10.1007/978-1-4020-6774-7_4.
- Screen, J. A., and I. Simmonds, 2010: Increasing fall-winter energy loss from the Arctic Ocean and its role in Arctic temperature amplification. *Geophys. Res. Lett.*, **37**, L16707, <https://doi.org/10.1029/2010GL044136>.
- , and R. Blackport, 2019: How robust is the atmospheric response to projected Arctic Sea ice loss across climate models? *Geophys. Res. Lett.*, **46**, 11 406–11 415, <https://doi.org/10.1029/2019GL084936>.
- , C. Deser, and I. Simmonds, 2012: Local and remote controls on observed Arctic warming. *Geophys. Res. Lett.*, **39**, L10709, <https://doi.org/10.1029/2012GL051598>.
- Serreze, M. C., A. P. Barrett, J. C. Stroeve, D. N. Kindig, and M. M. Holland, 2009: The emergence of surface-based Arctic amplification. *Cryosphere*, **3**, 11–19, <https://doi.org/10.5194/tc-3-11-2009>.
- Shu, Q., Q. Wang, Z. Song, and F. Qiao, 2021: The poleward enhanced Arctic Ocean cooling machine in a warming climate. *Nat. Commun.*, **12**, 2966, <https://doi.org/10.1038/s41467-021-23321-7>.
- , —, M. Årthun, S. Wang, Z. Song, M. Zhang, and F. Qiao, 2022: Arctic Ocean amplification in a warming climate in CMIP6 models. *Sci. Adv.*, **8**, eabn9755, <https://doi.org/10.1126/sciadv.abn9755>.
- Skagseth, Ø., T. Furevik, R. Ingvaldsen, H. Loeng, K. A. Mork, K. A. Orvik, and V. Ozhigin, 2008: Volume and heat transports to the Arctic Ocean via the Norwegian and Barents Seas. *Arctic-Subarctic Ocean Fluxes*, R. R. Dickson, J. Meincke, and P. Rhines, Eds., Springer, 45–64, https://doi.org/10.1007/978-1-4020-6774-7_3.
- Smedsrud, L. H., R. Ingvaldsen, J. E. Ø. Nilsen, and Ø. Skagseth, 2010: Heat in the Barents Sea: Transport, storage, and surface fluxes. *Ocean Sci.*, **6**, 219–234, <https://doi.org/10.5194/os-6-219-2010>.
- , and Coauthors, 2013: The role of the Barents Sea in the Arctic climate system. *Rev. Geophys.*, **51**, 415–449, <https://doi.org/10.1002/rog.20017>.
- Stroeve, J., and D. Notz, 2018: Changing state of Arctic Sea ice across all seasons. *Environ. Res. Lett.*, **13**, 103001, <https://doi.org/10.1088/1748-9326/aade56>.
- Sun, L., C. Deser, and R. A. Tomas, 2015: Mechanisms of stratospheric and tropospheric circulation response to projected Arctic Sea ice loss. *J. Climate*, **28**, 7824–7845, <https://doi.org/10.1175/JCLI-D-15-0169.1>.
- Timmermans, M.-L., 2015: The impact of stored solar heat on Arctic Sea ice growth. *Geophys. Res. Lett.*, **42**, 6399–6406, <https://doi.org/10.1002/2015GL064541>.
- , and J. Marshall, 2020: Understanding Arctic Ocean circulation: A review of ocean dynamics in a changing climate. *J. Geophys. Res. Oceans*, **125**, e2018JC014378, <https://doi.org/10.1029/2018JC014378>.
- van der Linden, E. C., D. Le Bars, R. Bintanja, and W. Hazeleger, 2019: Oceanic heat transport into the Arctic under high and low CO₂ forcing. *Climate Dyn.*, **53**, 4763–4780, <https://doi.org/10.1007/s00382-019-04824-y>.
- Vincent, W. F., and Coauthors, 2011: Ecological implications of changes in the Arctic cryosphere. *Ambio*, **40**, 87–99, <https://doi.org/10.1007/s13280-011-0218-5>.
- Wang, Q., and Coauthors, 2016: An assessment of the Arctic Ocean in a suite of interannual core-II simulations. Part II: Liquid freshwater. *Ocean Modell.*, **99**, 86–109, <https://doi.org/10.1016/j.ocemod.2015.12.009>.
- , and Coauthor, 2020: Intensification of the Atlantic water supply to the Arctic Ocean through Fram Strait induced by Arctic Sea ice decline. *Geophys. Res. Lett.*, **47**, e2019GL086682, <https://doi.org/10.1029/2019GL086682>.
- Wild, M., A. Ohmura, H. Gilgen, J.-J. Morcrette, and A. Slingo, 2001: Evaluation of downward longwave radiation in general circulation models. *J. Climate*, **14**, 3227–3239, [https://doi.org/10.1175/1520-0442\(2001\)014<3227:EODLRI>2.0.CO;2](https://doi.org/10.1175/1520-0442(2001)014<3227:EODLRI>2.0.CO;2).
- Winton, M., 2006: Amplified Arctic climate change: What does surface albedo feedback have to do with it? *Geophys. Res. Lett.*, **33**, L03701, <https://doi.org/10.1029/2005GL025244>.
- Woodgate, R. A., 2018: Increases in the Pacific inflow to the Arctic from 1990 to 2015, and insights into seasonal trends and driving mechanisms from year-round Bering Strait mooring data. *Prog. Oceanogr.*, **160**, 124–154, <https://doi.org/10.1016/j.pcean.2017.12.007>.
- , and K. Aagaard, 2005: Revising the Bering Strait freshwater flux into the Arctic Ocean. *Geophys. Res. Lett.*, **32**, L02602, <https://doi.org/10.1029/2004GL021747>.
- , T. Weingartner, and R. Lindsay, 2010: The 2007 Bering Strait oceanic heat flux and anomalous Arctic sea-ice retreat. *Geophys. Res. Lett.*, **37**, L01602, <https://doi.org/10.1029/2009GL041621>.
- , K. M. Stafford, and F. G. Pahl, 2015: A synthesis of year-round interdisciplinary mooring measurements in the Bering Strait (1990–2014) and the RUSALCA years (2004–2011). *Oceanography*, **28** (3), 46–67, <https://doi.org/10.5670/oceanog.2015.57>.
- Yeager, S. G., A. R. Karspeck, and G. Danabasoglu, 2015: Predicted slowdown in the rate of Atlantic Sea ice loss. *Geophys. Res. Lett.*, **42**, 10 704–10 713, <https://doi.org/10.1002/2015GL065364>.